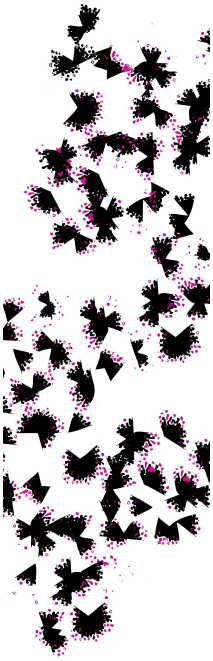

Acoustic impedance matching using 3D printed lenses

S.S. (Sangitha) Harmsen

BSc Report

Committee:
Prof.dr.ir. C.H. Slump
Prof.dr.ir. G.J.M. Krijnen
Martijn Schouten, MSc
Dr.ir. H. Wormeester

December 2018

045RAM2018
Robotics and Mechatronics
EE-Math-CS
University of Twente
P.O. Box 217
7500 AE Enschede
The Netherlands

UNIVERSITY OF TWENTE.

MIRA CTIT
BIOMEDICAL TECHNOLOGY AND TECHNICAL MEDICINE

Abstract

This bachelor thesis is an investigation into the optimal layer thickness and impedance profile for a multilayer anti-reflection ultrasound lens, based on simulations using the transfer matrix method. Simulation results show the biggest decrease in reflection for a discretised exponential impedance matching profile with layer thicknesses proportional to the corresponding sound speeds. The model is validated through measurements with relatively simple 3D-printed test structures. The comparison of simulation results to the measurements suggests that the model is valid for the measurement ranges used. Based on the characterisation results, it is not feasible to 3D-print an anti-reflection ultrasound lens with the currently available printer and materials; therefore the validity of the model to such a lens also has not been verified.

Contents

List of Symbols

This page contains an overview of the symbols used in this work, their associated meanings, and their units.

c	speed of sound ($\mathrm{m\,s^{-1}}$)
E	Young's modulus (Pa)
f	frequency (Hz)
G	shear modulus (Pa)
I	acoustic intensity ($\mathrm{W\,m^{-2}}$)
j	imaginary unit
k	wavenumber ($\mathrm{rad\ m^{-1}}$)
p	sound pressure (Pa)
Q	volumetric flow rate ($\mathrm{m^3\,s^{-1}}$)
R_a	amplitude reflection coefficient
R_I	intensity reflection coefficient
T_a	amplitude transmission coefficient
T_I	intensity transmission coefficient
v	particle velocity ($\mathrm{m\,s^{-2}}$)
z	specific acoustic impedance ($\mathrm{Pa\,m^{-1}\,s}$ or Rayl)
Z	acoustic impedance ($\mathrm{Pa\,m^{-3}\,s}$ or $\mathrm{Rayl\,m^{-2}}$)
α	attenuation coefficient ($\mathrm{dB\,m^{-1}}$ or $\mathrm{m^{-1}}$)
β	phase constant ($\mathrm{rad\ m^{-1}}$)
γ	propagation constant ($\mathrm{m^{-1}}$)
λ	wavelength (m)
ν	Poisson's ratio
ρ	density ($\mathrm{kg\,m^{-3}}$)
ω	angular frequency ($\mathrm{rad\ m^{-1}}$)

Chapter 1

Introduction

This report contains the documentation of a bachelor thesis. The thesis is an investigation into the optimisation of a multi material impedance matching structure, that can be used to reduce reflections of ultrasound waves at interfaces. In the report, the relevant theory is set up, followed by a derivation of the model and a selection of the simulation results. 3D printed test structures are used in an underwater ultrasound measurement setup for characterisation and model validation. The report ends with an overall discussion and conclusion.

1.1 Context

Ultrasound, which is sound at frequencies higher than 20 kHz, is widely used in many applications to examine and modify objects. Example applications include fault detection, heating in welding, and medical diagnosis. A mismatch in acoustic impedance at material interfaces causes portions of the wave to be reflected back, which leads to energy inefficiency, and less effective imaging and material modification. Repeated reflections at mismatched interfaces can also extend ultrasonic pulse duration, which decreases axial resolution [1].

For example, at a tissue-air interface, over 99% of an ultrasonic wave is reflected. To avoid this, gels or oils are used as couplants between the ultrasound transducer front face and the tissue, thereby eliminating the presence of an air layer [2]. Ultrasonic probes typically have a matching layer at the front face, with a thickness one quarter of the wavelength of the frequency for which the transducer is designed. One way to tune the impedance of the layer is by mixing high- and low-impedance polymers [3].

The development of piezoelectric materials in the highly electrostrictive ferroelectric relaxor family such as PMN-PT (lead magnesium niobate-lead titanate), which have wider frequency bandwidths than previously used materials, makes it desirable to also develop impedance matching structures with better spectral performance [4]. This bachelor thesis examines the possibilities of stacking multiple 3D-printed layers for impedance matching, and improving matching over a range of frequencies.

1.2 Related work

There are several works investigating the use of layered impedance matching structures. One example is by DeSilets et al., 1978 [5], in which an optimal two-layer impedance matching structure has layer impedances as shown in equation 1.1. Here, z_{mi} refers to the i^{th} matching layer's impedance, from left to right within the matching structure. To the left of this structure is z_L, i.e. the impedance of a piezoelectric material, and z_R is the load medium impedance on the right, such as water or the human body. These impedances are calculated from KLM (Krimholz-Leedom-Mattaei) equivalent circuit models of the transducer. Similarly, Souquet et al., 1979 [6] use a Mason equivalent circuit to calculate optimal impedance, which for one layer would be $(2z_L z_R^2)^{(\frac{1}{3})}$.

Some more recent works look into specific materials and manufacturing methods for such impedance matching structures. For example in the paper by Fang et al., 2018 [7], anodic aluminium oxide (AAO) is proposed as an improved material for one of two matching layers for a PZT-water coupling, using an epoxy for the other. The impedance values are based on layer impedances of equation 1.1. Manh et al., 2014 [8] propose a method for manufacturing impedance matching layers on a silicone wafer with MEMS technology, to create layer impedances in accordance with DeSilets (equation 1.1).

$$z_{m1} = z_L^{(\frac{4}{7})} z_R^{(\frac{3}{7})} \tag{1.1a}$$

$$z_{m2} = z_L^{(\frac{1}{6})} z_R^{(\frac{5}{6})} \tag{1.1b}$$

A different approach is using a genetic algorithm to determine layer impedances for multi-layer acoustic matching. Saffar et al., 2012 [9] use a Dijkstra genetic algorithm to determine optimal impedance layers, and are able to find closely matching impedances in a database of matching layer materials.

Another direction is the development of acoustic metamaterials and phononic crystals for impedance matching. Bai et al., 2018 [10] use 3D printed metamaterial structures, but their focus is on wavefront transformation. Li et al, 2017 [11] use a sub-wavelength cone structured metamaterial to create an impedance gradient for matching.

Continuous impedance gradients have also been studied in optics for antireflection coatings, of which a formative work is by Southwell, 1983 [12]. Recent continuations of this work include investigations into optic broadband anti reflection coatings (BBAR), such as by Matsuoka et al., 2018 [13].

1.3 Research goal

The goal of this work is to investigate the optimal layer impedance and thickness for an impedance matching structure, that couples two materials at a range of frequencies. The structure is to be 3D printed. The focus is on medical ultrasound applications. This involves frequencies between 1-15 MHz and load impedances around 1.5 MRayl, but the results may also apply to other ranges of frequencies and load impedances.

1.4 Approach

The approach taken is to develop a model for multiple layers based on transfer matrices, and investigate optimal scenarios. Measurements are carried out with 3D printed structures in an underwater ultrasound. The results are used to characterise the materials, and to compare to simulation results for model validation.

Chapter 2

Theory

What follows in this section is an introduction to ultrasound and a description of sound wave speeds and behaviour in different materials and at interfaces. This lays the ground work for describing and analysing what happens to the energy in a sound wave, in terms of transmission, reflection and absorption.

At a fundamental physical level, sound is the propagation of energy through matter as a wave , i.e. pressure variations arise from particle vibrations . Sound requires a medium to travel in. In fluids, sound waves travel as longitudinal waves of alternating compression and rarefaction. In solids, sound can also propagate as a transverse wave, with alternating regions of shear stress perpendicular to the direction of the wave. Solids also support other modes of sound propagation, such as surface waves. [14]

2.1 Ultrasound and its applications

Ultrasound concerns sounds at frequencies higher than 20 kHz. Ultrasound technologies have a wide range of industrial, scientific and medical uses. One way to categorise these applications is into low and high power. Low-power applications are generally focused on sensing and imaging, without altering the medium the waves pass through. Usually these involve frequencies in megahertz or higher, and powers up to a watt. Conversely, high-power applications, i.e. power ultrasonics, is used to alter chemical, physical or biological properties of objects, using up to thousands of watts and usually frequencies below 100 kHz. Figure 2.1 shows an overview of some of these applications and their corresponding frequencies.

High-power ultrasound may give rise to a number of significant nonlinear phenomena such as shock waves and harmonics generation. One such effect used in several applications is cavitation. This is when gas bubbles (cavities) form in a liquid during rarefaction of the sound wave. The bubbles may form from dissolved gases or the vapour of the liquid itself. When these bubbles expand, fragment or rupture, high localised temperatures and stresses arise, sometimes along with the creation of free radicals. These conditions are useful in sonochemistry and ultrasonic cleaning. Some other applications of power ultrasonics include welding of metals and polymers, emulsification, noninvasive surgery, atomisation of liquids, machining of brittle materials, and the formation and processing of nanomaterials. [16, p. 5] [17] The noninvasive surgery application is also referred to as high intensity focused ultrasound (HIFU) treatment. An example of this is using a high-power focused

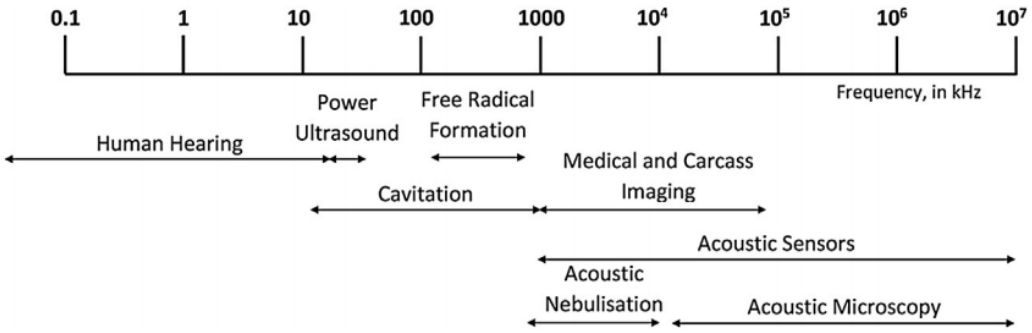

Figure 2.1: Frequency ranges of a number of ultrasound applications and acoustic phenomena [15].

ultrasound beam to rapidly heat a tumour in the kidney to above 55°C, while leaving the healthy tissue in the path largely unaffected. [18]

Among the low-power applications are nondestructive testing of materials, such as flaw detection in ceramics and metal sheets or pipes, and characterisation of materials, such as grain size. Other applications include medical imaging, and surface acoustic waves in electronics. One exception to the general trend of low-power imaging and detection is sonar, in which sound waves for underwater detection are used at a wide range of powers. SONAR stands for SOund Navigation And Ranging, and its specific uses include underwater detection of fish and navigation in submarines. Sonar frequencies may range from 10^2 to 10^6 Hz. [16, pp. 2,7]

2.1.1 Ultrasound transducers

Piezoelectric transducers are commonly used to generate ultrasound. Piezoelectricity is an effect in materials of a two-way relation between mechanical strain and electrical potential, due to an asymmetry in crystal structure. Quartz was found in early use as a piezoelectric material, but more recently common materials used include lead zirconate titanate (PZT) and lithium niobate.

A piezoelectric transducer probe typically consists of a layer of piezoelectric material with metal electrodes connected to two sides. The dimensions of the piezoelectric layer depend partly on the desired resonant frequency. When an alternating voltage is applied to these electrodes, the thickness of the layer varies with the electric field across it. Ultrasonic transducers are excited by voltages in the range of 10^2 V. The voltage may be sinusoidal (single-frequency) or a pulse containing various frequencies, and the energy conversion is most efficient at the piezoelectric element's resonant frequency. [19] [20]

As the piezoelectric effect works both ways, the same probe can also be used as a receiver, i.e. sound waves can be measured as varying voltage. As illustrated in Figure 2.2, the element can be damped with a backing material such as epoxy, to shorten the pulse width and improve axial image resolution. The front face may also include an acoustic matching layer to reduce reflections, as well as an acoustic lens to shape the beam. [16, pp. 175-177] [21, pp. 119-165] [22, pp. 79-112]

Single piezoelectric elements can also be combined in transducers in a number of ways to shape the beam. Sequenced arrays can be linear or curved, while phased arrays may be

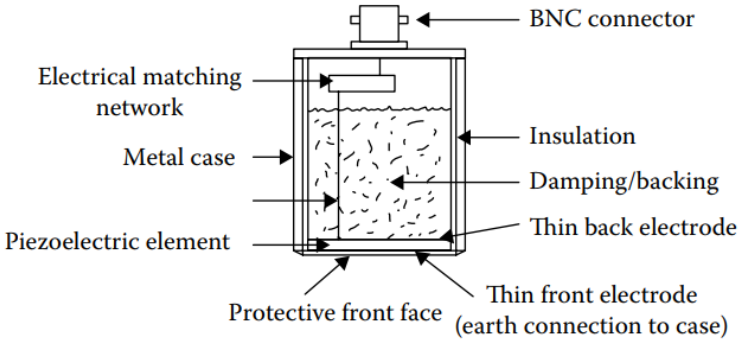

Figure 2.2: Basic structure of a piezoelectric ultrasonic transducer [16, p. 177].

linear or annular. The type of element arrangement and firing order affects the scan field and image shape. [23, pp. 540-542]

When the ultrasound wave passes through the finite aperture, the beam spreads in the medium beyond because of diffraction. By modelling the plane transducer as a cylindrical piston, a diffraction correction integral can be calculated for reflection or transmission spectra, incorporating focal length, sample distance and thickness, and transducer aperture radius. [24] [25]

Besides piezoelectric transducers, additional types also exist for generating ultrasound. One of these is the magnetostrictive transducer. Electrostriction is the slight displacement of ions in dielectric materials in response to an external electric field, and magnetostriction is the equivalent for magnetic materials in external magnetic fields. Other types of transducers include capacitive, electromagnetic, pneumatic and mechanical. Certain properties vary between these methods, such as higher displacement amplitude or velocity, or ability to operate at extreme temperatures. This may be useful depending on the application. [16, pp. 192-212] [22, pp. 119-148]

2.1.2 Medical ultrasound imaging

Medical ultrasound scanning is a form of non-invasive and real time imaging. At limited power-irradiation time combinations, this can be done without physically adverse effects, unlike with ionising radiation. Most human tissue has mechanical properties similar to a fluid, so the shear waves through such materials are negligible. The frequencies used in medical diagnoses generally lie between 1 MHz and 15 MHz. Higher frequencies are used for better resolution, but as this is accompanied by more attenuation, it is also limited to shallower depths. [22, pp.297-300]

Ultrasound images generally depend on one two principles: reflections at interfaces, and Doppler shifts from moving materials. Pulse-echo times and amplitudes are based on reflections. An ultrasonic pulse is emitted into the body; the time elapsed until an echo is received gives information about depth, while the amplitude of the echo gives information about the acoustic properties along the path.

The images can be shown in a number of modes. The simplest of these is an A-scan, which displays (amplified and rectified) receiver voltage against time. This is used in ophthalmology and encephalography. Another mode is B-scan, which is most common for

sonography. This is a two-dimensional representation of a more extended region, made from probing several locations with sound beams. Echo times determine pixel location, and their intensity determine the pixel brightness. The section of the image corresponds to a plane parallel to the beam direction.

M-mode contains temporal information: a line along a single location showing depth, and the other axis showing changes in these over time. This can track motion towards and away from the transducer. Finally, Doppler modes and variations of these are also common modes. Sound reflected on a moving medium undergoes a measurable frequency shift which depends on magnitude and direction of the movement. This technique is often used to measure blood-flow rates, or movements of certain organs such as the heart. [16, pp. 593-596]

2.1.3 Image artifacts

Several assumptions are made when reconstructing an ultrasound image in B-mode, and these contribute to image artifacts, i.e. misrepresentations in the image of what is scanned. Examples of these inconsistencies are omitting structures, and showing them in the wrong location, size or brightness. Some assumptions computing images are as follows. Sound is assumed to travel in a straight path, at a constant speed and return from the main beam after a single reflection. Additionally, acoustic energy is assumed to be attenuated uniformly along the path and the transducer is assumed to be the only source present. These assumptions can generally not be avoided, because the premise of imaging is to view internal structures of which the specifics are unknown.

The reverberation type artifact arises from multiple echos, which happens in the presence of two parallel, highly reflective surfaces. The echos are interpreted as multiple objects of increasing distance, when they are in fact the same. A ring-down artifact is a line or series of bands extending behind air bubbles, caused by resonant vibrations. Other artifacts occur due to attenuation which is in fact non-uniform. When a beam passes through a highly attenuating structure, the beam echos from parts further than this will also be weaker, and this causes shadowing on the image.

Non-ideal beam shapes also cause artifacts. Reflections are assumed to come from the main beam, with waves parallel to the main axis of the beam. However, side lobes and grating lobes, which are off-axis beam lobes, cause structures, sometimes referred to as ghosts, to wrongly appear as if originating from the main beam. Ghosting may also occur due to the differing speeds of sound in different materials. When a beam is obliquely incident, refraction occurs. The image, which assumes the wave path to be a straight line, may represent structures of the wrong width, or introduce phantom duplicates. [26] [27]

2.2 Sound wave intensity and attenuation

Acoustic intensity is the power transmitted by a sound wave per unit area perpendicular to the direction of wave propagation. It is defined as in equation 2.2, with particle velocity $\vec{v}$ and sound pressure p.

An acoustic particle is a conceptual particle large enough to encompass millions of molecules, but small enough that its acoustic variables can be considered nearly homo-

geneous. Particle velocity is the instantaneous velocity of acoustic particles; this means that the average velocity of the millions of molecules in the aforementioned particle is considered. Sound pressure is the instantaneous difference between equilibrium pressure and actual pressure, caused by the compressions and rarefactions due to the sound wave. [28] The equation describes the instantaneous intensity, which varies with time.

$$\vec{I}(t) = p(t)\vec{v}(t) \tag{2.1}$$

Hence, sound-intensity is a vector. However, in the remaining of the report we will use only single direction and therefore use:

$$I(t) = p(t)v(t) \tag{2.2}$$

where the direction is implied. For a sinusoidal waveform with sound pressure and particle velocity in phase, the average intensity is described in equation 2.3, where the zero subscripts denote amplitude.

$$I = \frac{1}{2}p_0 v_0 \text{ actually } \vec{I} = \frac{1}{2}p_0\vec{v}_0 \tag{2.3}$$

As a sound wave propagates through matter, it's amplitude and therefore its intensity decreases. In a uniform material, this can be described as an exponential decay with a frequency-dependent amplitude attenuation coefficient α, shown in equation 2.4. I_0 is the original average intensity at the coordinate $x = 0$. The factor 2 appears in the equation because intensity is proportional to the square of sound pressure (amplitude), which decays exponentially, and x is the distance travelled by the wave in the medium. Equation 2.5 shows the equivalent formulation for amplitude, i.e. for sound pressure. [29, p. 350]

$$I(x) = I_0 e^{-2\alpha(f)x} \tag{2.4}$$

$$p(x) = p_0 e^{-\alpha(f)x} \tag{2.5}$$

Beam divergence, scattering and stress-cycle hysteresis contribute to attenuation. Beam divergence is associated with spherical waves rather than plane waves. It occurs as the wave spreads over a larger area, causing the amount of energy per unit area to decrease. In heterogeneous media, non-uniformities such as grain boundaries or air bubbles cause energy to be deflected away from the beam, i.e. scatter. The effect is influenced by how the diameter of the obstruction compares to the sound's wavelength (and therefore, frequency). Additionally, energy is converted to other forms like heat in the stress cycles, due to hysteresis. This happens once every temporal cycle, so the loss scales proportional to frequency. In polymers, hysteresis may arise because of viscoelastic effects. The rise of scattering and hysteresis attenuation effects with an increase of frequency explains why higher-frequency sound beams of the same initial intensity would have a smaller penetrative depth in a given material. [16, pp. 72-78] [30]

In polycrystalline materials with average grain diameter $\bar{D}$, the attenuation coefficient for a planar wave (no beam divergence) is expressed in equation 2.6. The first term with coefficient B_1, is related to absorption, while the second relates to scattering. The effect of scattering depends on how the wavelength compares to the average grain diameter. In

the Rayleigh regime, the wavelength is significantly larger than $\bar{D}$, and the contribution of scattering to the attenuation is proportional to f^4, as shown in equation 2.7. For grain diameters roughly equal to the wavelength, the stochastic scattering attenuation coefficient is proportional to the square of the frequency. The final case is when wavelength is far smaller than average grain diameter, known as geometric or diffusion scattering. This is frequency-independent. The coefficients C_1, C_2 and C_3 are material-specific constants. [22, pp. 223-226] [31]

$$\alpha = B_1 f + \alpha_s \tag{2.6}$$

$$\alpha_s = \begin{cases} C_1 \bar{D}^3 f^4 & \lambda \gg \bar{D} \\ C_2 \bar{D} f^2 & \lambda \simeq \bar{D} \\ C_3 \bar{D}^{-1} & \lambda \ll \bar{D} \end{cases} \tag{2.7}$$

2.3 Sound velocity and mechanical material properties

In a homogeneous medium, sound velocity depends on physical properties of the medium and of the wave. These are the density and elastic properties of the medium; and frequency, amplitude and mode of the wave. The properties influence how quickly the displacement of one particle may propagate to its neighbours. Solids can contain more modes of acoustic waves than simply longitudinal because unlike fluids, they can sustain shear forces. Waves may also have different modes depending on whether they travel in the bulk or on the surface of a material. [16, p. 30]

The speeds of longitudinal and transverse waves in homogeneous, isotropic solids are expressed by the physical relations in equations 2.8 and 2.9 respectively [21, p. 19]. Here, E is the Young's modulus, G the shear modulus and ν the Poisson's ratio of the medium.

$$c_l = \sqrt{\frac{E}{\rho} \frac{1-\nu}{(1+\nu)(1-2\nu)}} \tag{2.8}$$

$$c_t = \sqrt{\frac{E}{\rho} \frac{1}{2(1+\nu)}} = \sqrt{\frac{G}{\rho}} \tag{2.9}$$

From equations 2.8 and 2.9, the ratio of longitudinal speed to transverse speed of a bulk wave in a solid can be calculated to be that of equation 2.10, depending only on the Poisson's ratio. Solids generally have a Poisson's ratio between 0 and 0.5, meaning that longitudinal acoustic waves travel faster than their transverse counterparts in such materials. The ratio of longitudinal to transverse speed goes to infinity for a Poisson's ratio going to 0.5.

$$\frac{c_l}{c_t} = \sqrt{\frac{2(1-\nu)}{1-2\nu}} \tag{2.10}$$

In anisotropic media, the speed of acoustic wave propagation depends on direction, and there is additional differentiation between polarisations of modes. In isotropic media, two independent elastic constants such as Young's modulus and Poisson's ratio, along with

density, are enough to calculate sound speed. Depending on the material, there may be up to 21 independent elastic constants required to calculate the phase and group velocities of sound waves in anisotropic solids. [32, p. 10]

2.3.1 Multi-frequency sound waves and dispersion

When a sound wave contains multiple frequencies, this might be an additional factor influencing the speed of sound. In a dispersive medium, the speed of propagation depends on frequency, in addition to the factors already discussed.

For a sound wave comprising multiple frequencies, it is necessary to distinguish between group and phase velocity. Phase velocity is the rate of spatial displacement of a particular phase, such as a pressure crest. Group velocity is kinematically defined as the velocity of the envelope of the wave. Figure 2.3 shows a simple example of a signal with three frequencies, with the equation $y = 2\sin 5x + 2\sin 5.5x + \sin 5.6x$. The rate of displacement of the envelope (yellow and orange lines) is the group velocity, while the rate of displacement of the amplitude crest marked by the red cross would be the phase velocity.

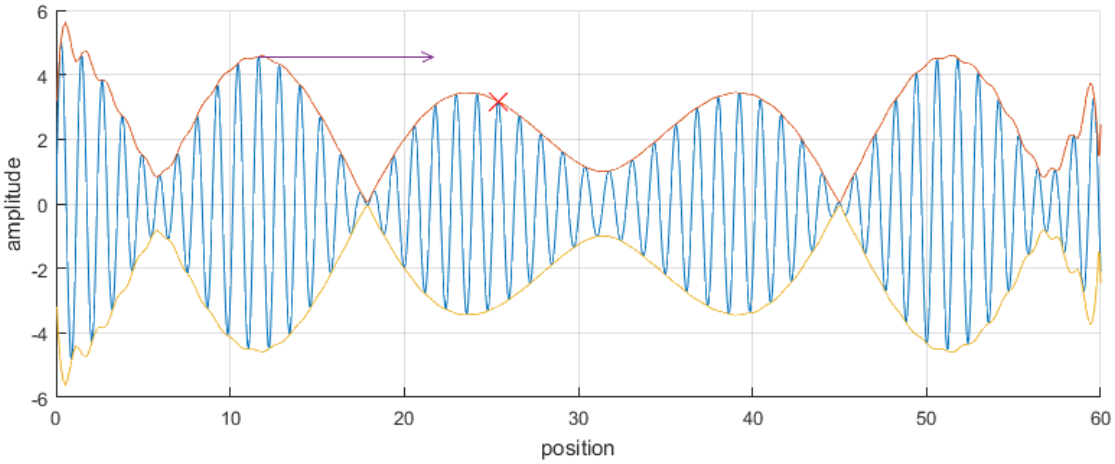

Figure 2.3: Representation of sound wave containing several frequencies, along with signal envelope.

The group and phase velocity are equal in non dispersive media, and unequal in dispersive media, where phase velocity depends on wavenumber (and therefore frequency). If the different frequency components of the wave travel with different velocities, then the overall shape of the wave also changes. This depends on the relationship between temporal and spatial frequencies. [33] The angular velocity ω and wavenumber k are related to frequency and wavelength through the relations in equations 2.11 and 2.12.

$$\omega = 2\pi f \tag{2.11}$$

$$k = \frac{2\pi}{\lambda} \tag{2.12}$$

A wave with angular velocity ω and wavenumber k has a phase velocity c_p as defined in equation 2.13.

$$c_p = \frac{\omega}{k} = f\lambda \tag{2.13}$$

For a wave comprising multiple frequencies within a narrow band, the amplitude of the wave train is modulated, i.e. wave packets arise. The velocity of these packets c_g is defined by the group velocity in equation 2.14, where the derivative is evaluated at the central wavenumber of the wave packet. [34]

$$c_g = \frac{\partial \omega}{\partial k} \tag{2.14}$$

By using $\omega = kc_p$ from equation 2.13 along with the product rule, equation 2.14 can be rewritten to equation 2.15. In nondispersive media, the group velocity equals the phase velocity and phase velocity is independent of frequency, while in dispersive media, group velocity depends on phase velocity and an additional term dependent on how phase velocity changes with the central wavenumber of the wave packet.

$$c_g = c_p + k\frac{\partial c_p}{\partial k} \tag{2.15}$$

In lossless media (which can be dispersive), group velocity equals the velocity at which energy and information is propagated. In absorptive media, group velocity is still defined as in equation 2.14, but c_g becomes a complex quantity which is not equal to the velocity of energy propagation [35]. For dissipative media, ω is differentiated with respect to the (real) central wavenumber of the wave packet. However, this central wavenumber shifts as the wave propagates, with the drift proportional to the imaginary part of $\frac{\partial \omega}{\partial k}$. [36]

In the model, the media shall be considered non dispersive and therefore the phase velocity equal to the group velocity, since velocity is considered independent of frequency in the materials used in this work for the relevant frequency ranges.

2.4 Time and frequency domain sound wave representations

The wave equation is a partial differential equation which describes the motion of waves, and the one-dimensional version is expressed in equation 2.16 for sound pressure propagating along the x dimension. In this case, $\tilde{c}$ represents the speed of sound, c. Any planar disturbance propagating with a constant speed c can be described as a function $f(x \pm ct)$. Using equation 2.13, it can be seen that this is equivalent to $f(kx \pm \omega t)$. When the propagation medium is lossless, k is the real wavenumber and the speed c is a real constant. [37, Ch. 47]

$$\frac{\partial^2 p}{\partial x^2} - \frac{1}{\tilde{c}^2}\frac{\partial^2 p}{\partial t^2} = 0 \tag{2.16}$$

In case the propagation material has damping, the same wave equation applies, but then $\tilde{c}$ is a complex number, sometimes referred to as the complex speed of sound. Here, a function of $f(\gamma j x \pm \omega t)$ satisfies this modified wave equation, where γ is related to the phase constant β and the attenuation coefficient α through equation 2.17. [38] The phase constant β in this one-dimensional situation is simply the wavenumber k.

$$\gamma = \alpha + j\beta \tag{2.17}$$

Equation 2.18 is a solution to the wave equation. In the chosen sign convention with $e^{j\omega t}$ rather than $e^{-j\omega t}$, it represents a right-travelling wave with amplitude A at x, $t = 0$ and a left-travelling wave with amplitude B at x, $t = 0$, along the x coordinate. The amplitude coefficients A and B may be complex. This wave has an angular frequency ω, and the x subscript for the γ value denotes that this is material-dependent, and may change over the coordinate.

$$p(x,t) = (Ae^{-\gamma_x x} + Be^{\gamma_x x})e^{j\omega t} \tag{2.18}$$

To illuminate the physical interpretation of this wave representation, the real part of the first term in equation 2.18 is a sinusoidal perturbation moving along positive x over increase in time, and showing an exponential decrease in amplitude over x, as expressed in equation 2.19. The B term is the same, except that it travels in the direction of negative x over time. Alternatively, a signal can also be written as the sum of $f(\gamma jx + \omega t)$ and $f(-\gamma jx - \omega t)$, which also results in a real sinusoid as in equation 2.19.

$$\mathrm{Re}\left[Ae^{-\gamma_x x}e^{j\omega t}\right] = A\cos(\omega t - kx)e^{-\alpha x} \tag{2.19}$$

Sound pressure and particle velocity are related through impedance, as expressed in equation 2.24. For a non-viscous medium in which the shearing stresses are zero, Euler's inviscid equation of motion in one dimension (perpendicular to gravitational acceleration such that it can be neglected) is expressed in equation 2.20. [39, p. 7].

$$\nabla p + \rho\frac{\partial \mathbf{v}}{\partial t} = 0 \tag{2.20}$$

Here, ρ refers again to the equilibrium density of the medium rather than the instantaneous deviations caused by the sound waves. Note that in equation 2.20, velocity is a three-dimensional vector. In the planar case being considered, there is only movement along the x-axis and the equation can be rewritten to only the x-axis in equation 2.21.

$$\frac{\partial p}{\partial x} + \rho\frac{\partial v_x}{\partial t} = 0 \tag{2.21}$$

Using these relations, the particle velocity corresponding to sound pressure expressed in equation 2.18 is given by equation 2.22. In case of attenuating materials, the complex speed $\tilde{c} = \frac{j\omega}{\gamma}$ is used, and the impedance is complex [40].

$$v(x,t) = \frac{1}{z_x}(Ae^{-\gamma_x x} - Be^{\gamma_x x})e^{j\omega t} \tag{2.22}$$

Since reflection, transmission and attenuation are highly frequency-dependent, it is useful to implement frequency analysis. The Fourier transform allows to transform from continuous time domain to continuous frequency domain, and is defined in equation 2.23. [41] Using this, the frequency representations of equations 2.22 and 2.18 are the same, except that the $e^{j\omega t}$ term is dropped. For the discrete-time measured data, discrete Fourier transforms can be used to analyse the frequency components of the data.

$$X(\omega) = \int_{-\infty}^{\infty} x(t)e^{-j\omega t}dt \tag{2.23}$$

2.5 Sound waves at material interfaces

When a wave encounters an interface between different media, its propagation is altered and the energy is redistributed in a manner that may involve phenomena such as refraction, scattering and reflection. This depends on the type of wave, the orientation of approach to the interface, and acoustic properties of the materials on either side of the boundary.

An important property to consider here is impedance, which relates how much force is required to induce a certain velocity change . It is a complex quantity which describes both magnitude and phase. Characteristic acoustic impedance is defined as in equation 2.24, where $\hat{p}$ is sound pressure and $\hat{v}$ is particle velocity. The sound pressure and particle velocity may be described in complex notation by their Fourier transforms, or as phasors. [39, pp. 41-48] Characteristic impedance can also be calculated from the speed of sound and material density. When complex speed is used, this results in complex impedance, but in the following measurements and simulations, the speed and impedance are taken to be real. Note that the density here refers to the equilibrium density, rather than the instantaneous local density caused by compressions and rarefactions of a sound wave. Using equations 2.3 and 2.24, average acoustic intensity can be rewritten as in equation 2.25 [29, p. 347], which applies to pressure and sound velocities in phase. For complex impedances, they are out of phase, and equation 2.2 is integrated over one period and divided by the period for the average intensity over time.

$$z = \frac{\hat{p}}{\hat{v}} = \rho\tilde{c} \tag{2.24}$$

$$I = \frac{p_0^2}{2z_0} \tag{2.25}$$

Another consideration for behaviour at interfaces is the shape of the wavefronts and of the boundary. The geometry determines, for instance, the angle of incidence and beam divergence. At rough interfaces, diffuse reflection rather than specular reflection occurs: the reflected wave scatters in numerous directions. Mathematical analyses often consider waves to be planar or spherical, meaning the surfaces of equal phase are parallel planes or concentric spheres respectively.

At a boundary, some energy is reflected back into the wave originating medium and some is transmitted. The angle of reflection equals the angle of incidence. Snell's law generalises to acoustic waves, to determine the angle of refraction of waves at boundaries. Snell's law is shown in equation 2.26. Here, θ_1 is the angle of incidence (in region 1), θ_2 the angle of transmittance (in region 2), and c_1 and c_2 represent the phase velocities of sound in the two media respectively, see Figure 2.4. The θ values are defined as the angles between the direction of wave propagation, and the normal to the boundary. [22, p. 40]

$$\frac{\sin\theta_1}{\sin\theta_2} = \frac{c_1}{c_2} \tag{2.26}$$

With the angles known, there are also relations to calculate the proportion of the wave that is reflected, and that which is transmitted. The following applies to planar waves at fluid-fluid boundaries, where pressure and velocity are continuous at the boundary. The reflection coefficient, defined as the ratio of the reflected amplitude to the amplitude of

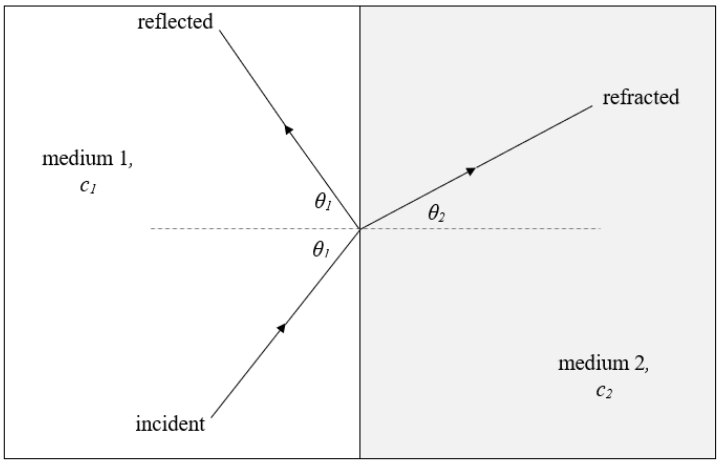

Figure 2.4: Wave reflection and refraction at a material interface with oblique incidence.

the incident wave, is described in equation 2.27. The transmission coefficient, defined as the ratio of the transmitted wave's amplitude to that of the incident wave, is described in equation 2.28. T and R depend on the impedance values of the boundary materials. These coefficients also apply to relative pressure amplitudes of the wave.

$$R_a = \frac{p_r}{p_i} = \frac{z_2 \cos\theta_1 - z_1 \cos\theta_2}{z_2 \cos\theta_1 + z_1 \cos\theta_2} \tag{2.27}$$

$$T_a = \frac{p_t}{p_i} = \frac{2z_2 \cos\theta_1}{z_2 \cos\theta_1 + z_1 \cos\theta_2} \tag{2.28}$$

At boundaries involving a solid on at least one side of the boundary, there may also be conversion of wave mode. For instance, an arriving longitudinal wave may be partially converted to a shear wave upon transmission into a solid. However, mode conversion does not occur at material boundaries for normally incident waves. [22, p. 43]

For a normally incident wave, the cosines drop out and the relations simplify to the following: $R = \frac{z_2 - z_1}{z_2 + z_1}$ and $T = \frac{2z_2}{z_2 + z_1}$. Reflection and transmission coefficients are also used to describe relative intensities. In this case, using equation 2.25, the reflection and transmission coefficients R_I and T_I for normally incident waves become as shown in equations 2.29 and 2.30, noting that this applies to media with real impedances. The subscripts i, r and t stand for incident, reflected and transmitted respectively. When considering intensities, $R_I + T_I = 1$ at any single interface, which holds with the conservation of energy.

$$R_I = \frac{I_r}{I_i} = |R_a|^2 = \left(\frac{z_2 - z_1}{z_2 + z_1}\right)^2 \tag{2.29}$$

$$T_I = \frac{I_t}{I_i} = |T_a|^2 \cdot \frac{z_2}{z_1} = \frac{4z_1 z_2}{(z_1 + z_2)^2} \tag{2.30}$$

2.5.1 Sound through multiple layered interfaces

When a sound wave passes through multiple successive interfaces, the behaviour compared to a single interface is complicated because reflection and transmission can occur between intermediate boundaries, potentially an infinite number of times. This scenario can be analysed using the transfer matrix method: relations between two variables at either end of a two-port system are described by a (complex-valued) matrix. This is also known as the Thomson-Haskell method. These matrices can be multiplied to describe end-to-end behaviour for several cascaded two-ports. This approach was developed for the electric and magnetic fields of electromagnetic waves in optics and electronics, but has been adapted to cover acoustic systems using pressure and particle velocity as state variables. [42] This is described below.

Let the sound pressure and particle velocity be described as planar waves travelling along x as expressed in equations 2.18 and 2.22. A non-slip boundary is assumed between materials, which means that both particle velocity and sound pressure are continuous at an interface. In that case, changes in particle velocity and sound pressure between two ends (subscripts 1 and 2) of a homogeneous layer of infinite extent, with acoustic impedance z_l can be described by the matrix relation in equation 2.31. This layer is assumed to have planar faces perpendicular to the wave. See Figure 2.5 for an illustration of what the matrix describes: the transformation of the pressure and particle velocity between points $x = x_1$ and $x = x_2$ by the layer with thickness d.

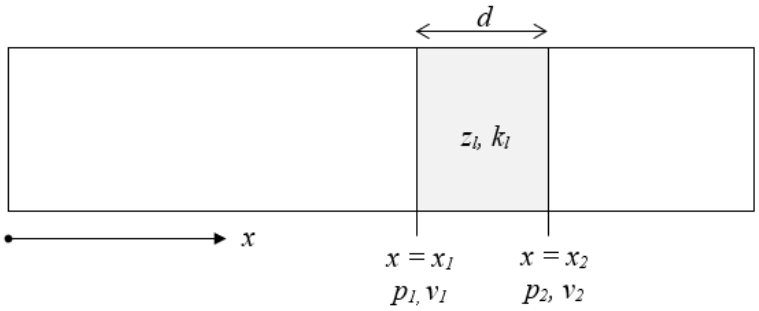

Figure 2.5: Sketch of single layer described by transmission matrix.

$$\begin{bmatrix} p_1 \\ v_1 \end{bmatrix} = \begin{bmatrix} A & B \\ C & D \end{bmatrix} \begin{bmatrix} p_2 \\ v_2 \end{bmatrix} = \begin{bmatrix} \cosh(\gamma d) & z_l \sinh(\gamma d) \\ \frac{\sinh(\gamma d)}{z_l} & \cosh(\gamma d) \end{bmatrix} \begin{bmatrix} p_2 \\ v_2 \end{bmatrix} \tag{2.31}$$

For isotropic and homogeneous media, the matrix is always symmetric, such that $D = A$. Note that p_1 and v_1 are to the left, i.e. to negative x of p_2 and v_2. If the positions were reversed, the only difference in the matrix would be the signs of the sinh terms. This is because the layer is a reciprocal two-port network: the determinant $AD - BC = 1$. This, along with symmetry, causes the inverse matrix to only have sign differences in B and C. [42] [43, pp. 53-57]

The matrix in equation 2.31 is for an attenuating medium. In lossless materials, the attenuation coefficient α is zero, and the propagation constant becomes purely imaginary. The hyperbolic trigonometric functions of equation 2.31 simplify to circular sin and cos functions, whose argument becomes βd, i.e. kd. This can be derived using relations in

equations 2.17 and A.1 (see Appendix A). The matrix in equation 2.32, shows this simplification, and it describes sound propagating through a lossless layer. [43, p. 55]

$$\begin{bmatrix} p_1 \\ v_1 \end{bmatrix} = \begin{bmatrix} \cos(k_l d) & j z_l \sin(k_l d) \\ \frac{j}{z_l} \sin(k_l d) & \cos(k_l d) \end{bmatrix} \begin{bmatrix} p_2 \\ v_2 \end{bmatrix} \tag{2.32}$$

This method can be extended to describe multiple successive layers of infinite extent by cascading the individual matrices as shown in equation 2.33. Here, M_i denotes the transfer matrix of the i^{th} layer. For N layers, the overall transfer matrix is the product of the N successive transfer matrices.

$$\begin{bmatrix} p_0 \\ v_0 \end{bmatrix} = M_1 \begin{bmatrix} p_1 \\ v_1 \end{bmatrix} = M_1 M_2 \cdots M_i \cdots M_N \begin{bmatrix} p_N \\ v_N \end{bmatrix} = \begin{bmatrix} M_{11} & M_{12} \\ M_{21} & M_{22} \end{bmatrix} \begin{bmatrix} p_N \\ v_N \end{bmatrix} \tag{2.33}$$

Using the overall transfer matrix, transfer and reflection coefficients can be found. One way to do this is to assume an anechoic termination beyond the final layer, i.e. no reflected wave in the final medium. The transmission and reflection coefficients describe all portions of the wave transmitted and reflected from the various interfaces within, over time. The frequency domain representations contain all of the time information for each frequency, and therefore it is relevant to consider the frequency spectra of these coefficients.

The amplitude reflection and transmission coefficients of a planar wave incident on a layered structure are illustrated in Figure 2.6. Note that this is the frequency representation, independent of time (see Section 2.4). On the left, the incident wave with amplitude p_0 is travelling in positive x direction. The reflected wave with amplitude reflection coefficient R contains all the portions of the wave reflected at any of the multiple interfaces, at any point of time. Similarly, the transmitted term on the right describes all portions of the wave transmitted through the structure, after any combination of internal reflection and transmission. In the right side, any left-travelling wave is considered negligible. The transmission and reflection coefficients can be found from the transfer matrix values and the impedances of the left and right (z_L and z_R) media as shown in equations 2.34 and 2.35 [44]. Here, L is the total distance between the layers. The reflections follow the same path as the incident wave, but are shown shifted to distinguish them in the schematic.

$$R_a = \frac{z_R M_{11} + M_{12} - z_L z_R M_{21} - z_L M_{22}}{z_R M_{11} + M_{12} + z_L z_R M_{21} + z_L M_{22}} \tag{2.34}$$

$$T_a = \frac{2 z_R e^{j k_R L}}{z_R M_{11} + M_{12} + z_L z_R M_{21} + z_L M_{22}} \tag{2.35}$$

2.5.2 Optimal impedance profiles

Also in optics, antireflective coatings are studied. One type of these are gradient-index (GRIN) coatings, in which the refractive index of the coating changes along its profile. The refractive index is related to the speed of light in a material and is therefore comparable to acoustic impedance. In the work by Gomez et al (1966) [45], exponential index profiles in GRIN rods are explored. More recently, quintic (fifth-order polynomial) and Gaussian profiles frequently occur in literature. One example is the work by Leem et al. (2013) [46],

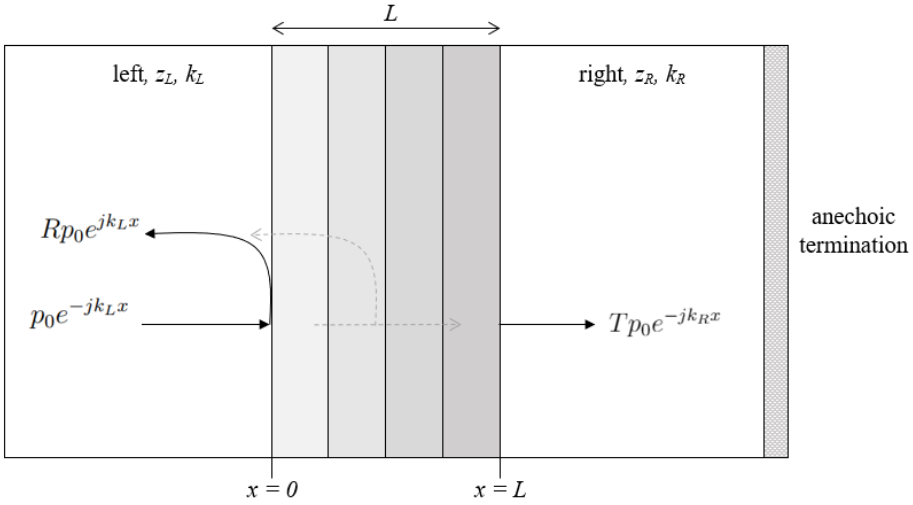

Figure 2.6: Schematic depiction of pressure waves through layered media with anechoic termination.

in which amorphous germanium films are manufactured using glancing angle deposition to create linear, quintic and Gaussian index profiles.

When materials of known impedance are mixed to create profiles of a property, the resulting impedance of the mix needs to be determined. There exist some rules to predict properties of mixes based on the properties of the constituent materials, such as Lichtenecker's logarithmic rule to predict electrical permittivity [47]. However, such a general rule does not seem to be available for acoustic impedance. Additionally, in this work, the proportions of materials used in the experimental mixed materials are unknown, so they are to be determined experimentally regardless.

In acoustics, continuously changing impedance profiles can be found in horns, which are also used to match impedances. Ultrasonic horns are typically cylindrical, tapered, exponential or stepped in their shape [48]. In the work by Roes et al. (2013) [49], stepped exponential horn shapes are explored for use in acoustic energy transfer applications.

Chapter 3

Simulation

For simulation in MATLAB, the transfer matrix method was implemented in increasing complexity, to individually investigate the effect of impedances, layer thickness and damping, followed by combinations of the same in multiple intermediate layers.

3.1 Single-layer simulations

First, a single, lossless layer between two different media was simulated. At a layer thickness of $\frac{\lambda}{4}$, there is maximum or minimum transmission depending on whether the layer impedance lies inside or outside of the range of the left and right material impedances; the quarter wavelength optimal thickness for impedance matching is an established result [50]. The behaviour of the system is also periodic in thickness over $\frac{\lambda}{2}$, which corresponds to a periodicity of π in the trigonometric parameter kd.

The optimal impedance for transmission is $z_c = (z_L z_R)^{\frac{1}{2}}$. This is derived in Appendix C.2 for a quarter-wavelength lossless layer. Figure 3.1 shows the transmission and reflection coefficients for varying layer impedance, including the optimum. Note that z_L and z_R values here are interchangeable, and the result is similar for any $z_L \neq z_R$. When the layer impedance is between z_L and z_R, the transmission is always higher than when there is no layer. Conversely, when the layer impedance is outside of this range, transmission is always lower.

The focus of this work shall be on the intensity transmission coefficient, as it relates to the energy of the incident wave that is transmitted, while less importance is placed on the phase and amplitude. However, a brief simulation and discussion of the amplitude transmission and reflection coefficients of a single, lossless layer can be found in Appendix D.2.

Next, the implications of damping are considered. In simulation, hyperbolic sines and cosines are used with complex wave propagation parameters. A result of this for a single layer with optimal layer impedance is shown in Figure 3.2, with left and right impedances at 1.5 MRayl and 15 MRayl respectively. In this plot, the damping coefficient is $100\,\mathrm{m}^{-1}$ and the results are plotted for a layer thickness of up to 12 times the wavelength.

The figure verifies the feasibility of the model in a number of ways. At zero thickness,

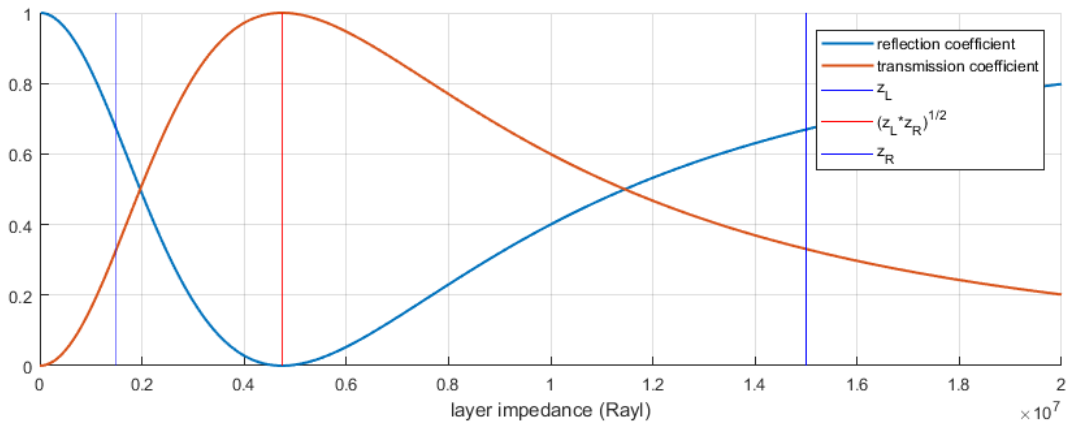

Figure 3.1: Simulated T_I and R_I values for various layer impedances, at layer thickness $\frac{\lambda}{4}$.

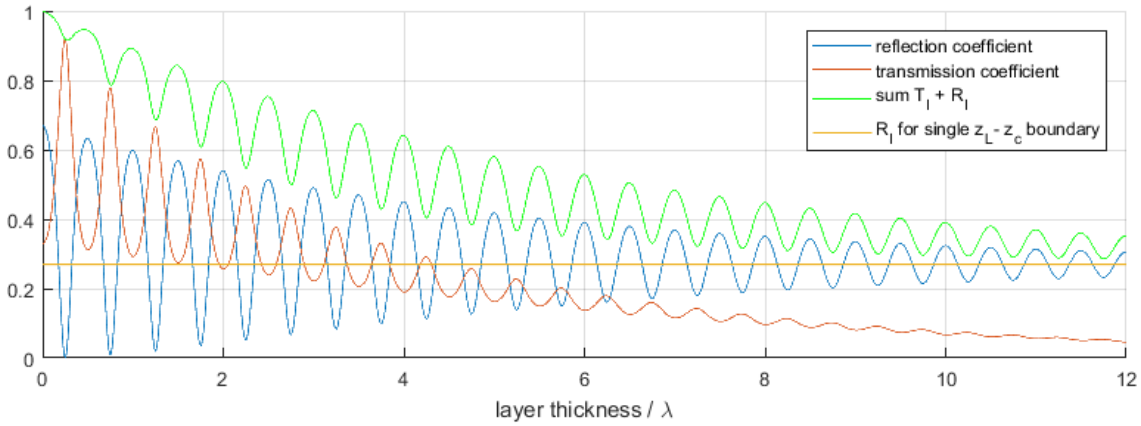

Figure 3.2: Effect of damping on R_I and T_I for various thicknesses of a single layer, with $\alpha = 60\ \mathrm{m}^{-1}$ and $\lambda = 1 \times 10^{-3}\,\mathrm{m}$.

the sum of reflection and transmission coefficient equals 1, which is expected because the surrounding medium is considered lossless. Both the reflection and transmission (intensity) coefficients show oscillations which damp out with an increase in thickness. The envelope of this damping is exponentially decaying.

With an increase in layer thickness, the transmission coefficient goes to zero because all the energy is eventually absorbed in the attenuating layer. The reflection coefficient goes to the value of reflection coefficient for a single interface between the left medium and the medium of the layer, as calculated from equation 2.29 and plotted in yellow. Another observation is that the sum of reflection and transmission does not decay as a smooth exponential. Rather, it oscillates with transmission peaks corresponding to minima in sum of transmission and reflection. This also makes sense because with more transmission, more energy is also converted to other forms due to attenuation within the layer. The main consequence from considering damping is that it is beneficial to choose smaller layer thicknesses for attenuating materials if the objective is to maximise energy transmission.

3.2 Multiple attenuating layers and orientations

A two-layer sample is simulated, to investigate the effect of reversing the orientation of the sample on the transmission and reflection coefficients. In the case of a lossless layer, there is no difference in the spectra of the transmission and reflection coefficients if the order of the layers is reversed. However, in case of attenuating materials, this does make a difference as illustrated in Figure 3.3.

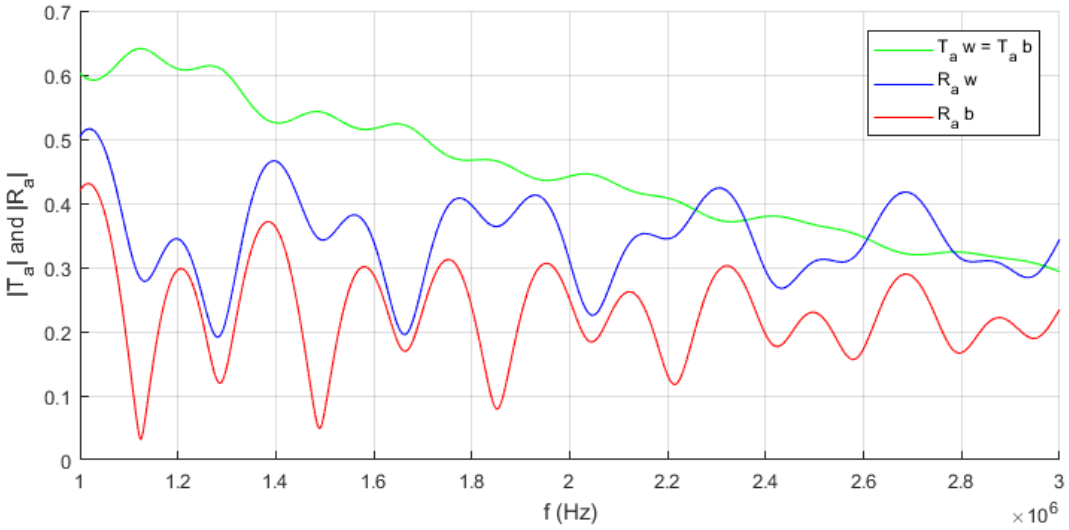

Figure 3.3: Simulated transmission and reflection coefficients for a two-layered sample in water, in forward and reverse orientation.

The simulation is done with parameters for a two-layered block of VeroWhite and Agilus Black each 3.0 mm, surrounded by water on both sides (see Tables 4.3 and B.1). It is simulated in the frequency range 1-3 MHz, to be able to compare to measurements. The layers are simulated as lossy, with attenuation coefficients as linear functions of frequency: $\alpha = -30 + 55 \times 10^{-6} f$ for VeroWhite and $\alpha = 10 + 75 \times 10^{-6} f$ for Agilus Black. The coefficients $T_a w$ and $R_a w$ are the absolute values of the amplitude reflection and transmission coefficients for the VeroWhite layer being closer to the transmitting probe, i.e. the leftmost layer in Figure 2.6. $T_a b$ and $R_a b$ represent the reverse situation, with Agilus Black closer to the transmitting transducer.

The simulation results show that the transmission coefficient is unaffected by this, but the reflection coefficients show different behaviour. When the black side is towards the transmitting probe, the reflection coefficient is lower. In fact, at higher frequencies, the transmission coefficient goes to zero as noted for a single attenuating layer, but the reflection coefficients go to the value of the single interface between water and the material closest to the transmitting probe, as elaborated on in Section D.3 of the Appendix.

3.3 Multiple layer simulations

3.3.1 Two layers and effect of kd

When two layers are placed between the left and right media, the behaviour depends on the thickness of each layer compared to the wavelength within that layer (determined by the speed of sound in that layer), as well as the layer impedance. Considering the lossless case, optimal transmission ($T_I = 1$) occurs when the impedance of any medium is the geometric mean of the adjacent impedances, i.e. the square root of the product at certain periodic layer thicknesses. In terms of the left and right impedances, it means that $z_1 = z_L^{\frac{2}{3}} \cdot z_R^{\frac{1}{3}}$ and $z_2 = z_L^{\frac{1}{3}} \cdot z_R^{\frac{2}{3}}$ for the first and second layers respectively.

The other consideration is layer thickness. For any i^{th} layer, the value $k_i d_i$ is equivalent to the thickness-to-wavelength ratio, scaled by 2π, see equation 3.1. The wavelength is determined by the speed of sound in the medium, and by scaling the thickness of each individual layer to the same proportion of the wavelength (e.g. $d_i = \frac{1}{4}\lambda_i$), the value of $k_i d_i$ is the same for different layers. However, when this value is not the same between different layers, the periodicity as well as the amplitude of the intensity transmission coefficient over different layer thicknesses behaves differently. This is plotted in Figure 3.4, for optimal layer impedances, and $z_L = 1.5$ MRayl, $z_R = 45$ MRayl.

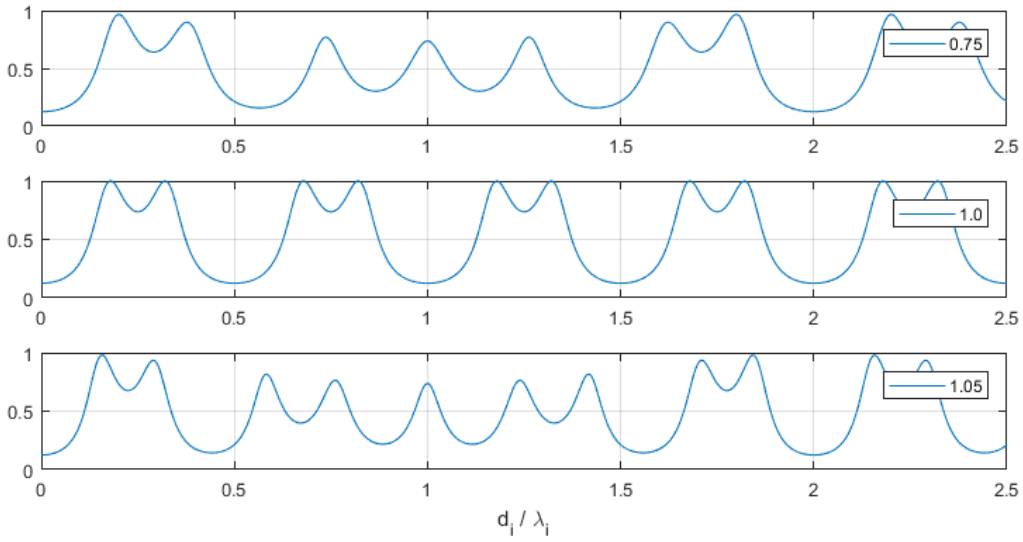

Figure 3.4: Different ratios of $k_2 d_2$ to $k_1 d_1$ for two lossless layers of optimal impedance, with both layer thicknesses scaled to λ_1.

The legend shows the ratio of kd of the second layer to the first layer. Difference in kd between layers may arise for example when thickness of both the layers is the same while the speed of sound and therefore wavelength is different by the factor in the legend. The x-axis shows the thickness of each layer, scaled by wavelength in the first layer. When kd is the same for both layers, the periodicity is, like with a single layer, still $\frac{\lambda}{2}$, but there are two peaks with value 1 instead of a single peak when there was just one optimal layer. For unequal kd, the periodicity is different and the peak values also drop below 1. Note that even for a difference factor of 1.05 in kd, there are visible shifts in the peak locations

and heights. As higher transmission is the objective, the case of matching kd values will be considered more desirable than the case in which they differ between layers.

$$k_i d_i = 2\pi \left(\frac{d_i}{\lambda_i} \right) \tag{3.1}$$

Additionally, scaling in sample thickness $\frac{d_i}{\lambda_i}$ can also be alternatively interpreted as scaling in normalised frequency $\frac{f}{f_0}$. Here, f_0 depends on the fixed thickness d, where $f_0 = \frac{c}{d}$, i.e. the sample thickness equals the wavelength corresponding to the normalising frequency. This means that thickness-scaling simulation results are equivalent to frequency-scaling simulation results.

N layers

For a structure with n intermediate layers between the left and right materials, the optimal impedance z_i of the i^{th} layer is given by the expression in equation 3.2. This still maintains that any layer's impedance is the geometric mean of the adjacent material impedances. In other words, using 3.2, it can be verified that $z_i = (z_{i-1} z_{i+1})^{\frac{1}{2}}$.

$$z_i = z_L^{(\frac{n+1-i}{n+1})} z_R^{(\frac{i}{n+1})} \tag{3.2}$$

The relation in equation 3.2 can also be expressed exponentially. That is, the optimal layer impedances are on locations along an exponential fit between the two end media, with the distribution of points depending on the number of layers. For n layers, the exponential form is shown in equation 3.3. The function expresses the impedance of the (integer) layer number x, and it is found by determining the exponential function which equals z_L for $x = 0$, and z_R for $x = n + 1$.

$$f(x) = z_L e^{\left(\frac{1}{n+1} \ln \left(\frac{z_R}{z_L} \right) x \right)} \tag{3.3}$$

Figure 3.5 shows the optimal layer impedances for a transition from 1.5 MRayl to 45 MRayl with 50 intermediate layers of impedances from equation 3.2, and the exponential fit satisfying equation 3.3.

The optimal result is when kd is the same value between different layers, and each layer has this optimal impedance: the number of T_I peaks in each period of $d = \frac{\lambda}{2}$ equals the number of layers. Furthermore, for a larger number of peaks, the transmission coefficient tends to remain closer to 1, except when the thickness values are a multiple of $\frac{\lambda}{2}$. As there are more peaks for more layers, the transmission coefficient stays closer to 1. These results are shown in the plot of Figure 3.6. The legend shows the number of optimised layers in the structure. This is for a left impedance of 1.5 MRayl and right of 45 MRayl, i.e. quite comparable to the interface between water and steel. It shows that for 100 layers of the optimal impedance, the intensity transmission is close to 1 for any thickness except for the sudden ripple and dip around multiples of half-wavelength thickness. Without this layered impedance matching structure, the intensity transmission coefficient from the left to the right medium would be 0.125.

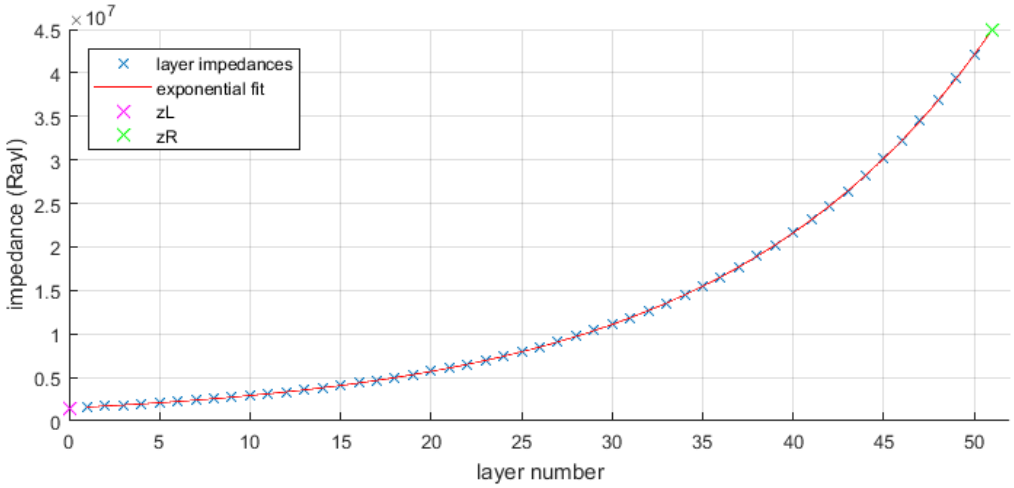

Figure 3.5: Exponential fit of the layer impedance transition for 50 layers between 1.5 MRayl and 45 MRayl.

All these simulations so far have been for a particular frequency (which has a particular wavelength in each material). However, from equations 2.13 and 3.1, the x-axis values could also be interpreted as $\frac{f}{f_0}$ instead of $\frac{d_i}{\lambda_i}$, where f_0 is a frequency for which each layer thickness equals the wavelength of the sound at that frequency. This means that this simulation describes a lens with certain optimal impedance values, of which the layer thickness scales with the speed of sound in that layer, and transmission could be near 1 for all frequencies except close to multiples of $\frac{f_0}{2}$ for a certain f_0 which determines the absolute layer thickness values.

There is not, of course, one single optimal impedance assignment for the layers, as this depends on a number of other factors. For example, when there are only two layers and a high but flat spectral response is required, the DeSilets impedances may be considered optimal, as from equation 1.1. The plot in Figure 3.7 shows a comparison for a two-layered structure between end impedances of 1.5 MRayl and 30 MRayl, with kd matched between the layers. The plot shows intensity transmission coefficient for the DeSilets impedances, and for those optimised with equation 3.2. While DeSilets has a more consistent spectral performance, the exponential optimal impedances have two higher peaks (of total transmission) in the same range. This might be better in two cases: when high transmission of narrow frequency spectrum is required, or when it is possible to create a structure with this impedance distribution but a larger number of layers.

3.3.2 Errors in optimal impedance values

It is practical to consider how the simulation is affected when the impedances of the layers are not exactly the optimal value. In the simulation, noise was introduced by adding Gaussian noise to each layer's optimal impedance, with mean zero and standard deviation a fixed percentage of that layer's optimal impedance. Results for 5% and 10% are plotted in Figure 3.8. Comparing this to the 20-layer case in Figure 3.6, it can be seen that 10% especially has a large effect, with transmissions dipping below 0.5 where they were over 0.97 in the noiseless case.

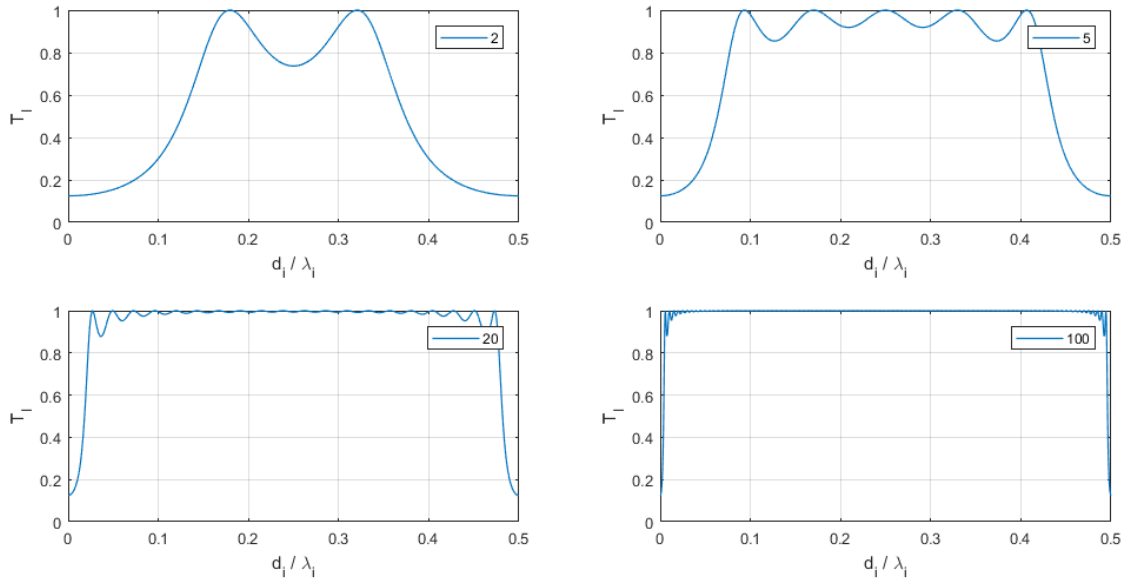

Figure 3.6: Simulations for different number of intermediate lossless layers with optimal impedances, for different thickness-to-wavelength ratios.

3.4 Model discussion and conclusion

The model has a number of merits and limitations, which are discussed below. To restate the main assumptions, the model applies to planar sound waves at normal incidence, passing through isotropic, homogeneous media. These media are also successive planar layers. The model can account for signal frequencies, layer thickness, material impedances, attenuation varying with frequency and the ordering of layers. It can be used to calculate the spectral reflection and transmission coefficients. These spectral reflection and transmission coefficients can be used to calculate the time domain response to a known input, using inverse Fourier transforms.

In practice, the geometry might be a good approximation in some cases, such as with planar immersion transducers as the one used. However, the model itself does not account for beam shaping, focusing and non-planar beams. This makes the model especially unsuitable to near-field predictions. The model applies to normal incidence of the ultrasound wave, but it can be extended to oblique incidence, which would also make the transmission and reflection coefficients dependent on the angle of incidence. The model also assumes planes of infinite extent. For samples significantly larger than the wavelength, this is a reasonable assumption. There exist methods to incorporate finite structure sizes, which is more applicable at lower frequencies [51], but this was not applied in this work.

Another limitation of this work is that only longitudinal waves were considered. At normal incidence, this is a valid assumption. At oblique incidence, other modes of sound waves are present within the solids, particularly shear waves. However, it is also possible to extend the model to include other modes of transmission. In that case, the state vector would have more states - one for each wave type in the medium (for both forward and backward directions). [52]

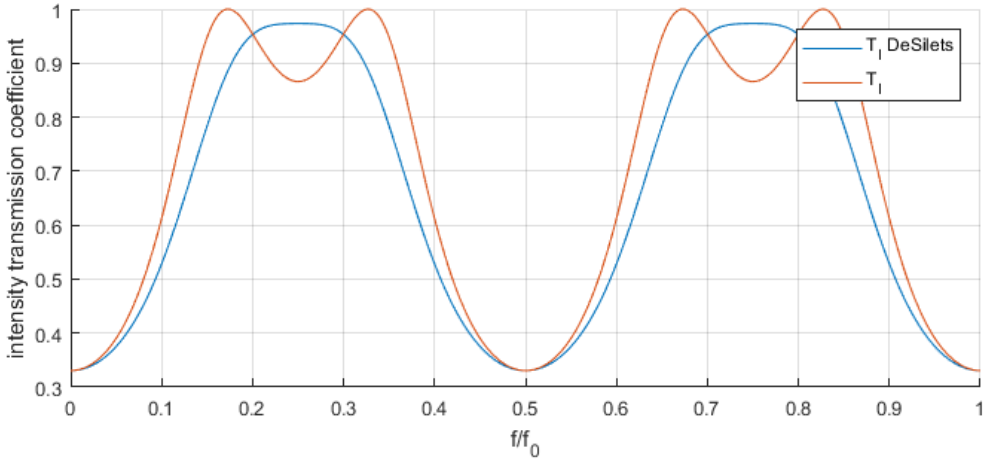

Figure 3.7: Simulations showing comparisons of intensity transmission coefficients for different optimal two-layered impedance matching.

One drawback of this method is that the numerical answers become less stable for higher frequencies and/or larger layer thicknesses. This instability arises from the limited accuracy of finite-arithmetic computers in evaluating the exponential terms. An alternative is proposed by Dazel et al. (2013) [53], but this has not been looked into further in this work.

3.5 Conclusions

From the simulation results, it is desirable that any antireflection structure is thin, as any extra thickness contributes to attenuation. The other main conclusions from the simulations are as follows. For optimal reductions in reflection of a planar wave, a layered transition between two media needs to meet two criteria: the layer thicknesses need to be proportional to the speed of sound within each layer, and the layer impedances need to follow a discretised exponential distribution between the two end materials. With a larger number of layers, the transmission coefficient has a flatter and wider optimal band in the frequency spectrum.

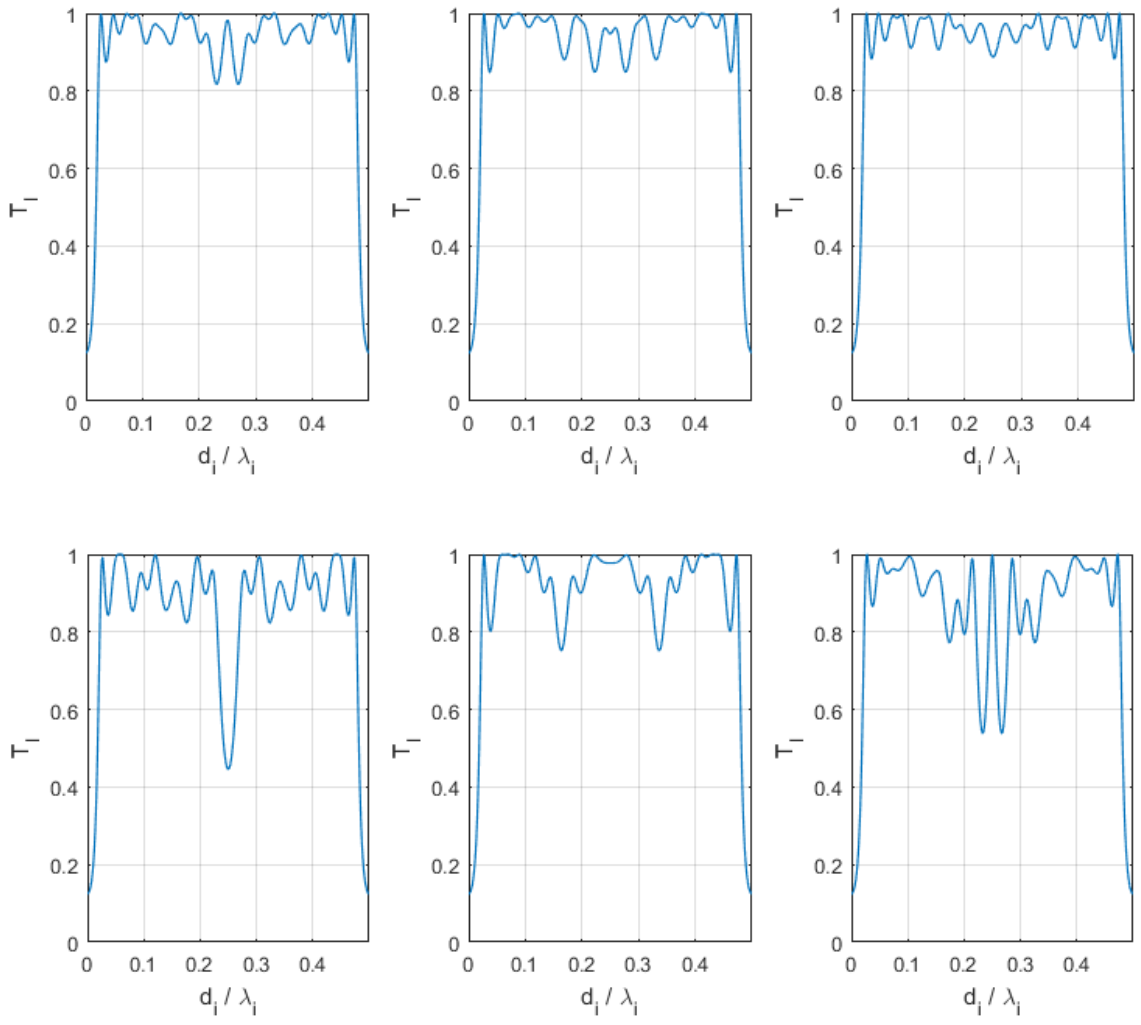

Figure 3.8: Plots of 20 layers with thicknesses scaled to layer wavelength, and noise introduced as a percentage of the optimal layer impedance value. The top three images show 5% Gaussian noise in each impedance value, and the bottom three show 10%.

Chapter 4

Measurements

This section concerning the experiments is structured as follows. First, the measurement setups, equipment and materials are described, in addition to specifying which data is measured and recorded. Then, the measurement data processing methods are described to show how meaningful values are extracted from raw data. Finally, the results of these processed measurement data are presented. This is followed by a discussion on the measurements themselves, and the results in context of the whole work are discussed further on in Chapter 5.

4.1 Experimental setup and measurement data

4.1.1 3D Printer: Objet Eden260VS

The 3D printer used in this work is the Objet Eden260VS, from Stratasys Ltd. It uses PolyJet technology: to build layers, the print head deposits drops of liquid photopolymer on the build tray, which are then cured by UV light to polymerise them. In the printer coordinate system, layers are added in the xy plane, along built up along the z-axis.

The x and y-axis resolution of the printer is 600 dpi (236 pixels per cm, $\approx 42\,\mu m$ per dot) and the z-axis resolution is 1600 dpi (630 pixels per cm, , $\approx 16\,\mu m$ per dot). The accuracy is 20 µm to 85 µm for features smaller than 50 mm and up to 200 µm for full model size. [54]

The printed samples are dimensioned to suit the clamps for the water tank. These are 50.0 mm × 50.0 mm across, with thicknesses of 4.0, 6.0 or 10.0 mm. This last dimension is the one along which ultrasound pulses are directed. Samples were printed to characterise the pure and combined materials, and finally a set of layered samples to verify the model.

Given the complexity and cost of the printer, the samples themselves were printed by a professional operator. The parts were designed in SolidWorks, and were sent as SLDPRT and STL files along with material requirements to be printed.

4.1.2 3D print materials

Two pure materials are available for use, along with several predetermined combinations of these two. These are VeroWhite and Agilus30Black, which is also referred to as Agilus Black. VeroWhite is a rigid white polymer, while Agilus Black is flexible and black. Twelve combinations of the two are available, of which the exact proportions are not made known by Stratasys. Other custom combinations would be demanding, as the material of every individual voxel (3D pixel) needs to be programmed, and this was not followed up within the scope of this work.

To investigate any significant anisotropy arising from the inherent asymmetry of 3D printing, two samples of pure Agilus black were printed: one with the short side along the z-axis of the printer and the other with the short side along the x-axis. The third sample was one of pure VeroWhite, with the short side along the z-axis. In each of these cases, the short side is the direction of measurement, along which the ultrasound wave is transmitted during measurements, while the axes in this section refer to those of the printer.

A second set of samples was printed to characterise all available materials. At least one sample of each material (two pure and twelve combinations) was printed, along with a second sample of different thickness for selected materials. The final set of samples comprised a two-layer sample of 0.3 mm VeroWhite and Agilus Black each, and three samples of five layers each, with the same combination of materials but with different individual layer thicknesses.

4.1.3 Underwater ultrasound setup

Several parameters of the materials need to be be entered in the simulation. These are density, speed of sound, acoustic impedance, attenuation and layer thickness. Measurements are made using an underwater ultrasound setup to determine speed of sound and attenuation. There are two variations of this setup: a pulse-echo mode and a through-transmission mode. Both of these are illustrated schematically in Figure 4.1, while photographs can be seen in Appendix F.1.

The setup includes a tank filled with distilled water, with plugged slots on each of the four sides for ultrasound probes to be inserted. The probes themselves are connected to a wave pulser using coaxial cables, and the probe signals are measured by a digital oscilloscope. A laptop is connected to the oscilloscope to view and log the measurements. In pulse-echo mode as shown in Figure 4.1a, the same ultrasound transducer is used for both sending and receiving pulses. In this case, the reflected pulses are measured. In through-transmission mode as in Figure 4.1b, two different probes are used. The T probe transmits a pulse, and the receiver probe measures the wave that passes through the sample. In this case, only the receiver probe signal is read by the oscilloscope. Table 4.1 shows the specific equipment used in this setup.

The square wave pulser was set to pulser voltage of 100 V and a pulse repeat frequency of 100 Hz. It also has a broad frequency setting, which is set to match the probe used. The probes were available for certain frequencies as two types: focused and unfocused. Focused beams converge up to a focus point, after which they diverge, while unfocused beams diverge more along the length of the beam. The focused probes used have a focal length of about 5 cm, see Table 4.1. In the part names in table, F stands for focal length

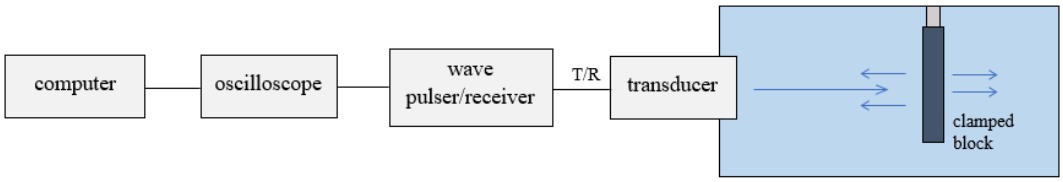

(a) Pulse-echo mode.

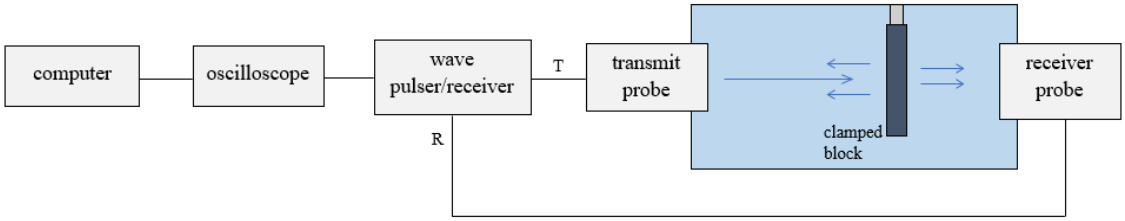

(b) Through-transmission mode.

Figure 4.1: Illustration of the pulse-echo measurement setup.

Table 4.1: An overview of the types and names of equipment used underwater ultrasound setup.

square wave pulser/receiver	Panametrics-NDT Model 5077PR
digital oscilloscope	Link Instruments DSO 8500
ultrasound immersion transducer	Panametrics-NDT V306 2.25 MHz/0.5" F = 1.9" PTF
ultrasound immersion transducer	Panametrics-NDT V306 2.25 MHz/0.5"
ultrasound immersion transducer	Panametrics-NDT V309 5 MHz/0.5" F = 2.00" PTF

and PTF stands for point target focus. This means the focus is a point rather than a line. Focused and unfocused probes were used of the 2.25 MHz type, while only focused probes were used for 5 MHz. In through-transmission measurements, two probes of the same type were used for consistency. The probes are single-element longitudinal transducers, with a quarter-wavelength layer for impedance matching to water. [55]

The samples were placed in stainless steel clamps, and were hung along a rail of which the distance is marked (see Appendix F.1, Figure F.1). At normal incidence of ultrasonic waves, the amplitude of reflections is maximised. For each measurement involving a sample, the mode was first set to pulse-echo and the angle of the sample was adjusted carefully by rotating the clamp, until the reflections had maximum amplitude. This ensures the incidence is as close to normal as possible.

4.1.4 Measurement logging

Throughout the measurements, the oscilloscope was set to a sampling frequency of 500 MHz, i.e. time intervals of 2 ns. The trigger voltage was adjusted with individual measurements

to keep the measured voltage within the measurement range of the scope, as measured amplitudes varied with distances and materials involved. Depending on the chosen memory size, the number of measurements logged is 262026 or 1048458. Each measurement set was exported as a CSV consisting of time and voltage values, to be processed further in MATLAB.

The dimensions of samples were measured using Vernier calipers, but there were significant uncertainties in the dimensions due to the dependence of the measurement on the manually applied force, especially for the more flexible materials. Instead, the dimensions sent to the printer were taken to be correct, and used in further calculations. It would be interesting to know the difference and variability to get an idea. For the densities, samples were weighed with a scale of 3 decimal points resolution in grams.

4.2 Data processing

4.2.1 Speed of sound

The speed of sound can be determined from the time difference between reflections from the front and back face of a sample, i.e. time-of-flight. This time difference is the time taken for sound to travel twice the thickness of the sample. For sound speeds, samples of a single layer were hung in the tank and pulse-echo measurements made. However, manually identifying the start of successive reflections is unreliable, while matching the difference between peaks is also not consistent because of the distortion in phase and waveform between reflections. The frequency-dependent reflection coefficient of the sample contributes to the distortion of the reflected waveform.

In the work by Cutard et al. (1993) [56], the use of analytic signals is found to be more reliable to determine group velocities than conventional phase slope and simple auto correlations methods. In this method, first the analytic signal is calculated for the relevant portion of the voltage measurements. This portion is manually identified for each probe-sample distance to include the first front and back face reflections. The Hilbert transform of a function $x(t)$ is defined in equation 4.1 [57]. The analytic signal comprises the original signal as the real part, and the Hilbert transform as the imaginary as shown in equation 4.2, where $V_a(t)$ is the analytic signal of the voltage, $V_r(t)$ is the real voltage from measurement and $H\left[V_r(t)\right]$ is the Hilbert transform of the measured voltage. The absolute value of the analytic signal is the envelope of the measured voltage.

$$H\left[x(t)\right] = \frac{1}{\pi}\int_{-\infty}^{\infty}\frac{x(\tau)}{t-\tau}d\tau \tag{4.1}$$

$$V_a(t) = V_r(t) + j \cdot H\left[V_r(t)\right] \tag{4.2}$$

To then determine the group velocity, the autocorrelation is calculated for the absolute value of the analytic signal, i.e. the voltage envelope. A peak in this autocorrelation corresponds to the time difference between the successive reflections [56]. It is worth noting that since the material is considered nondispersive in the model, it is sufficient to determine group velocity and consider the phase velocities to be equal to this.

4.2.2 Attenuation coefficient

Because the attenuation coefficient is highly frequency-dependent, a spectral method is used to determine the attenuation from measurement. First, frequency domain notation as introduced in Section 2.4 is established for the Fourier transforms of various measurements. Let $F_w(d)$ represent the frequency transfer function of a wave passing through water over distance d, as determined by the propagation constant of water. This is shown in equation 4.3.

$$F_w(d) = e^{-(\alpha_w + j\beta_w)d} \tag{4.3}$$

Similarly, for a sample with thickness d, attenuation coefficient α and phase constant β, the frequency transfer function can be expressed as $F_s(d)$ in equation 4.4.

$$F_s(d) = e^{-(\alpha + j\beta)d} \tag{4.4}$$

Figure 4.2 defines distances and signal paths for a set of measurements. Let U_w, U_s, U_1 and U_2 represent the Fourier transforms of the measured voltages of four different measurements: transmission without a sample, transmission with sample, front reflection from sample and back reflection from sample. The diagram shows the paths of U_s, U_1 and U_2. U_w would have the same path as U_s, except that the sample is removed from the water tank first.

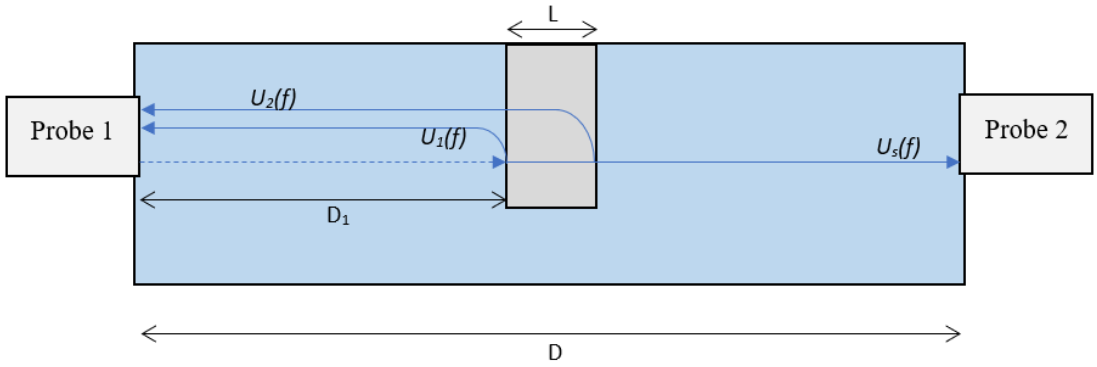

Figure 4.2: Schematic showing distances and signal paths for selected ultrasound measurements.

Table 4.2: Transfer functions for selected measurements, in frequency domain.

signal	frequency representation
$U_w(f)$	$U_0(f)F_w(D)$
$U_s(f)$	$U_0(f)F_w(D-L)F_s(L)\cdot T_{ws}T_{sw}$
$U_1(f)$	$U_0(f)F_w(2D_1)\cdot R_{ws}$
$U_2(f)$	$U_0(f)F_w(2D_1)F_s(L)\cdot(T_{ws}R_{sw}T_{sw})$

Table 4.2 shows the frequency transfer functions for the measurements U_w, U_s, U_1 and U_2, using the functions for water and the sample as defined in equations 4.3 and 4.4.

Here, T_{ws}, T_{sw} and R_{ws} represent amplitude transmission and reflection coefficients for the water-sample interface, as they describe the wave at one single interface and point of time rather than the overall transmission and reflection coefficients, which describe the wave behaviour across the whole structure for all successive reflection and transmission combinations. [40] $U_0(f)$ represents the Fourier transform of the combined effect of the transmit and receive probes, including their coupling lenses to the water.

In every section of the path, the wave is modified depending on the attenuation and phase constant in the material, and the distance travelled in that material. If A_i represents the amplitude of the corresponding U_i from equation 4.2, then the sample attenuation can be determined as shown in equation 4.5. [58]

$$\alpha = \frac{1}{L} \ln \left(\frac{A_1}{A_2} \cdot \frac{A_s}{A_w} \right) \tag{4.5}$$

In calculating attenuation coefficients, the relevant time sections of the measured voltage are selected manually for each of the waves in equation 4.2. The voltages are padded with zeros until they are all equal in length, so that any element wise operations on their Fourier transforms are for matching frequencies.

The above method was found to result in significantly different attenuation coefficients for different measurements with the same material. A possible reason for this is the spreading of the ultrasound beam, i.e. the diffraction due to the wave passing through the aperture of the probe opening. Therefore, the spectra of the various measurements are also divided by the Lommel diffraction correction integral, using an aperture radius of 1.27 cm. [24] [25]

4.2.3 Reflection and transmission coefficients

The transmission and reflection coefficients are ultimately used to compare the predictions of the model using parameters from the characterisation measurements, to investigate how well the model describes the measurements in reality.

The transmission and reflection coefficients can be calculated by dividing transmission and reflection spectra by the spectrum reference measurement without a sample. [59] To illustrate this, Figure 4.3 shows a schematic depiction of the complex functions which contribute to magnitude and phase changes of the ultrasound wave at each frequency. Figure 4.3a represents the setup with two probes facing each other in the tank, and a sample placed midway between them. Figure 4.3b is the same setup, but without the sample.

P_1 and P_2 represent the functions of the transmitting and receiving probes respectively. This includes the excitation pulse, the behaviour of the piezoelectric element and the coupling to the water. In a transmission pulse measurement, $P_1(f)$ and $P_2(f)$ are two different probes, so they may be different, while in a reflection pulse, the same probe is used for both transmission and reflection, so P_1 would equal P_2.

Next, $W(f, x)$ describes the effect of water. This includes any frequency-dependent spreading of the ultrasound beam, reflections off the wall, dispersion in water, and attenuation. This is also a function of x, i.e. the distance that the wave travels in this section. In Figure 4.3b, this is the entire distance between the two probe faces. In case of Figure 4.3a, this is the distance from the probe face to the surface of the sample. Assuming that the sample is placed halfway between the probes, the effect of water on either side of

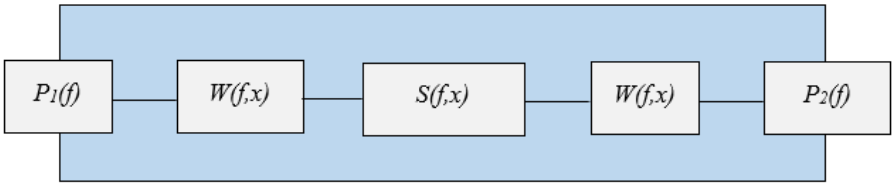

(a) Underwater ultrasound system diagram with sample.

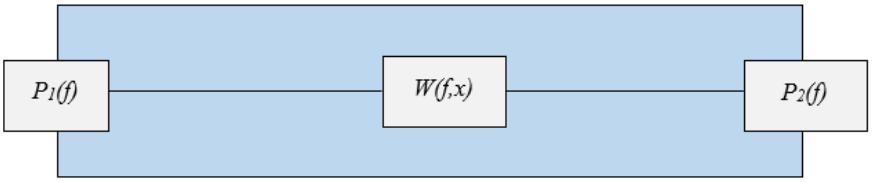

(b) Underwater ultrasound system diagram for reference without sample.

Figure 4.3: Schematic representations of the complex functions contributing to the spectrum of the measured ultrasound signals.

the sample can be considered identical, because it is along an axis of symmetry of the water tank.

Finally, $S(f, x)$ describes the effect of the sample on the wave. When this includes the spectrum of all transmitted or reflected signals, rather than for example only first front or back reflections in the attenuation calculations, this function describes the overall transmission or reflection coefficient. This in turn depends on frequency, sample thickness, attenuation, dispersion and scattering effects.

By dividing the frequency spectrum of a measurement in setup of Figure 4.3a by that of setup in Figure 4.3b, the frequency spectrum of the reflection or transmission coefficient can be calculated, depending on which probe is selected to receive the signal. One difference between the two setups is that a section of the path through water is different by a distance of the sample thickness i.e. the reference pulse passes through slightly more water than the pulse going through the sample. However, this effect is considered negligible, i.e. referring to Figure 4.2, $D \approx 2D_1$.

4.3 Measurement results

4.3.1 Characterisation results

To calculate the speed of sound, reflection measurements were used. A plot of an example of the measured reflected signal is shown in Figure 4.4. This is for a 10.0 mm thick sample of VeroWhite suspended about 9 cm from the probe in pulse-echo mode, in the water tank. The probe is used in the 2.25 MHz frequency range.

A number of observations can be made from this image. The first waveform starting around 1.44×10^{-4} s is a reflection from the front face of the block, while the next waveform starting 1.52×10^{-4} s is the portion of the wave reflected from the back face of the sample.

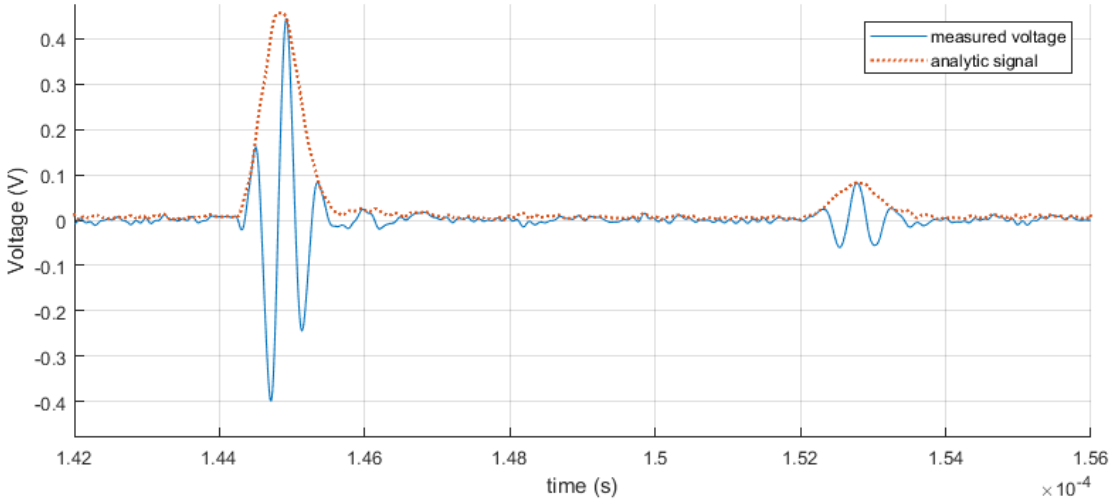

Figure 4.4: First front and back reflection measured with a 10.0 mm VeroWhite sample at 2.25 MHz, along with the absolute value of the corresponding analytic signal.

It can be seen that the waveform is distorted between the two reflections, and that the amplitude of the back reflection is also significantly smaller. This is due to frequency-dependent reflection and attenuation.

The dotted line in the figure shows the absolute value of the analytic signal, calculated as described in Section 4.2. Note that the peak of the analytic signal does not necessarily correspond to the positive peak of the voltage measured. Rather, it describes the envelope of the sinusoid which includes the negative peaks as well. The autocorrelation of this dotted line results in a peak at the time-of-flight, from which the group velocity of the sound is calculated.

Table 4.3 shows a summary of the characterisation results, i.e. the speed, density and impedance for each material. In total, there are 14 materials available to be characterised. This includes the two pure materials VeroWhite and Agilus Black, and 12 combinations of various proportions of them (of which the proportions are not published by Stratasys). When results for all of them are presented, they are ordered in increasing rigidity, from Agilus Black to VeroWhite.

Figure 4.5a shows a plot the speeds calculated from the pulse-echo measurements as described in Section 4.2.1. It can be seen that there is a general increase in the sound speed with an increase in rigidity. However, there is an exception for the fourth material, which corresponds to FLX9860-DM. This anomaly may be due to noise or mislabelled data, or there may indeed be an exception to the trend. Due to restricted access to measurement equipment this was not re-investigated after its discovery.

In the figure, the error bars are calculated from the standard deviations of the measurements. However, due to time constraints, several of the speed values are based on only two sets of measurements. Some of the materials have more repeats because there were two blocks of the same material, but different thicknesses.

Using the speed of sound (group velocity) and the density calculated for each material, the impedances were calculated. Figure 4.5b shows a plot of the resulting impedances, again

Table 4.3: Overview of characterisation results.

Number	Name	Speed ($\mathrm{m\,s^{-2}}$)	Density ($\mathrm{kg\,m^{-3}}$)	Impedance (MRayl)
1	AgilusBlack	2063.2	1116.5	2.30
2	FLX9840-DM	2087.7	1120.2	2.34
3	FLX9850-DM	2110.6	1136.0	2.40
4	FLX9860-DM	2144.5	1140.4	2.45
5	FLX9870-DM	2116.5	1143.4	2.42
6	FLX9885-DM	2173.2	1138.9	2.48
7	FLX9895-DM	2232.2	1158.4	2.59
8	RGD8530-DM	2459.5	1166.1	2.87
9	RGD8525-DM	2482.4	1176.2	2.92
10	RGD8520-DM	2488.7	1175.9	2.93
11	RGD8515-DM	2499.5	1176.9	2.94
12	RGD8510-DM	2501.3	1175.8	2.94
13	RGD8505-DM	2497.9	1177.8	2.94
14	VeroWhite	2523.5	1186.0	2.99

with the materials ordered from flexible to rigid and the material numbers corresponding to those in Table 4.3.

From Figure 4.5b, the shape is quite similar to the distribution of the speeds, as plotted in 4.5a. The material impedances range from about 2.3×10^6 Rayl to 3.0×10^6 Rayl. There is not much variation, especially in the RGD materials (numbers 8 to 13). Material 4 shows a slight exception to the trend, but this is from the anomaly in the speed for the same material . No extensive error analysis was performed due to the relatively small number of measurements for each sample, and due to time constraints.

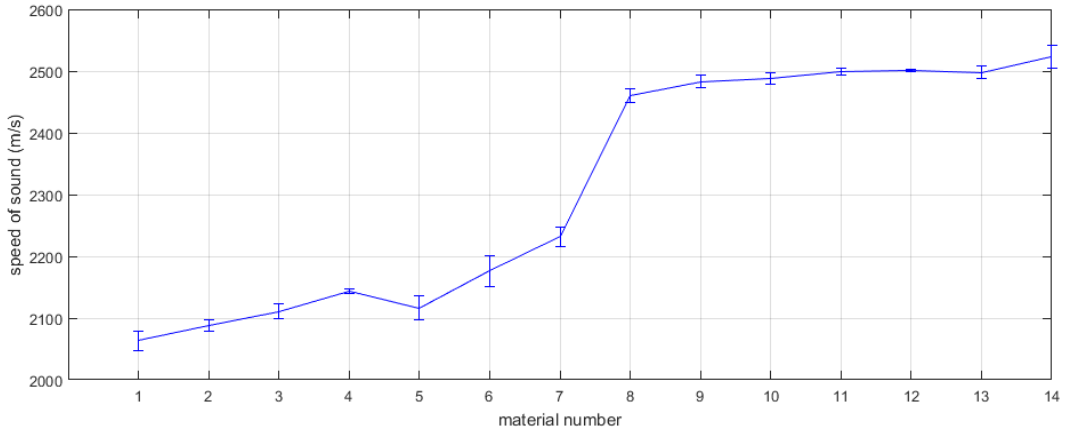

(a) Plot of speed of sound calculated from measurements for each of the pure and combined materials.

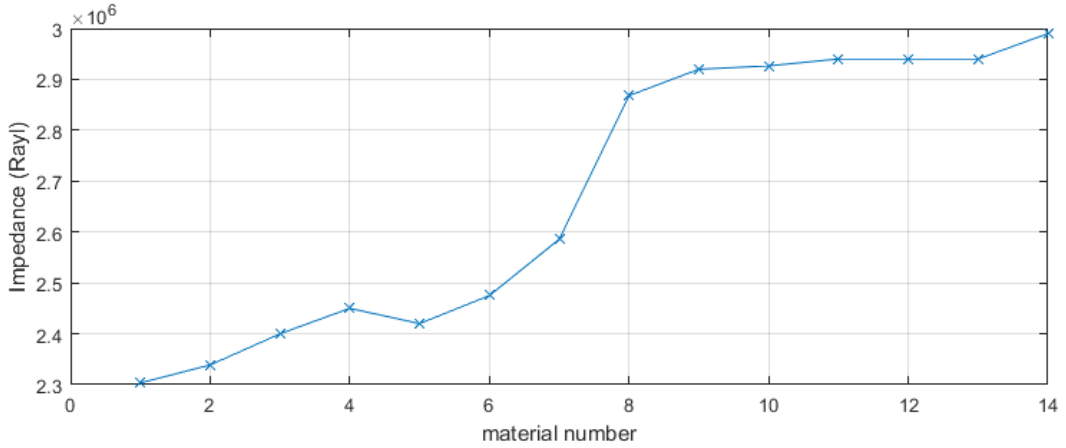

(b) Plot of speed of characteristic impedances calculated from speed and density for each of the pure and combined materials.

Figure 4.5: Characterisation plots of speed and impedance for the different materials.

Next, it was attempted to calculate attenuation coefficients as described in Section 4.2.2, but these were quite inconsistent for different measurements of the same material. Figure 4.6 shows an example of the mean α values from five measurements with the material RGD8520-DM, along with error bars determined from the unbiased standard deviation. The five measurements are:

1. 10.0 mm block along short dimension of the tank with focused 2.25 MHz probes
2. 6.0 mm block along short dimension of the tank with focused 2.25 MHz probes
3. 10.0 mm block along long dimension of the tank with focused 2.25 MHz probes
4. 6.0 mm block along long dimension of the tank with focused 2.25 MHz probes
5. 10.0 mm block along short dimension of the tank with unfocused 2.25 MHz probes

The relevant frequency range is the range for which the probe signals are stronger, approximately from 1.4-3.0 MHz (see Figure 4.7). In this range, α is chosen to be approximated as

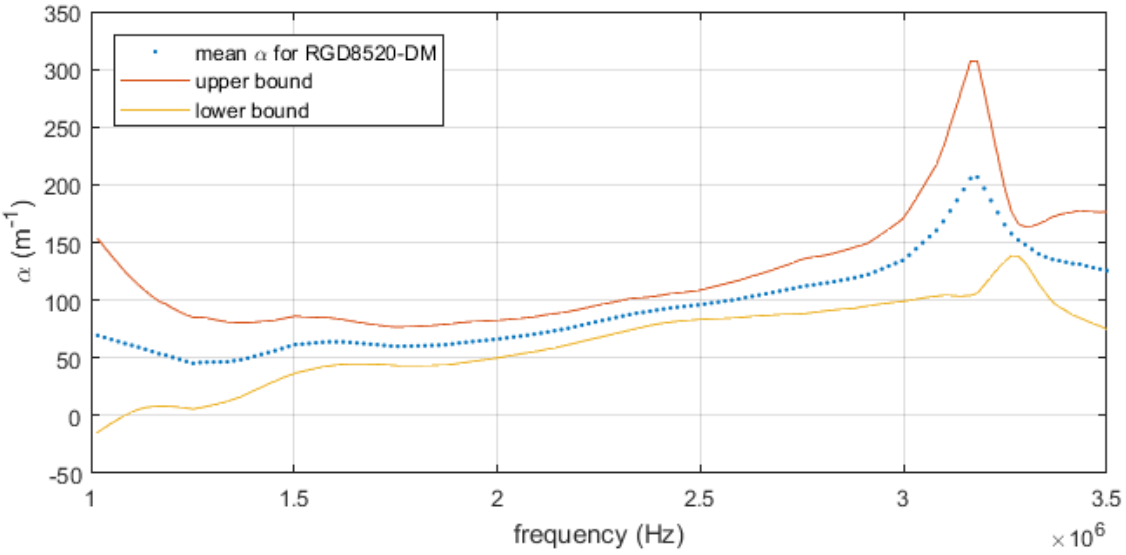

Figure 4.6: Plot of speed of characteristic impedances calculated from speed and density for each of the pure and combined materials.

a linear function of frequency. The five different measurements had unequal measurement section lengths and therefore values for unequal frequencies, so these were interpolated at 150 common frequencies to calculate the mean and error bars.

However, the error margins are still too large to be used in the simulation. In simulation, a difference in α slope or intercept of even 1 can make a significant difference in fit, while the error margins from the calculation lie in the order of tens. Additionally, most of the other materials have fewer relevant measurements to use, as a single attenuation calculation requires front and back reflection measurements, as well as transmission with and without the sample, which was constrained by time available.

4.3.2 Validation results

Reflection and transmission coefficients are calculated to compare to the model predictions for the same parameters. These are calculated in the frequency domain, and use references of transmission measurements without the sample. It was discovered that different probes of the same type have significantly different frequency characteristics. Figure 4.7 illustrates this.

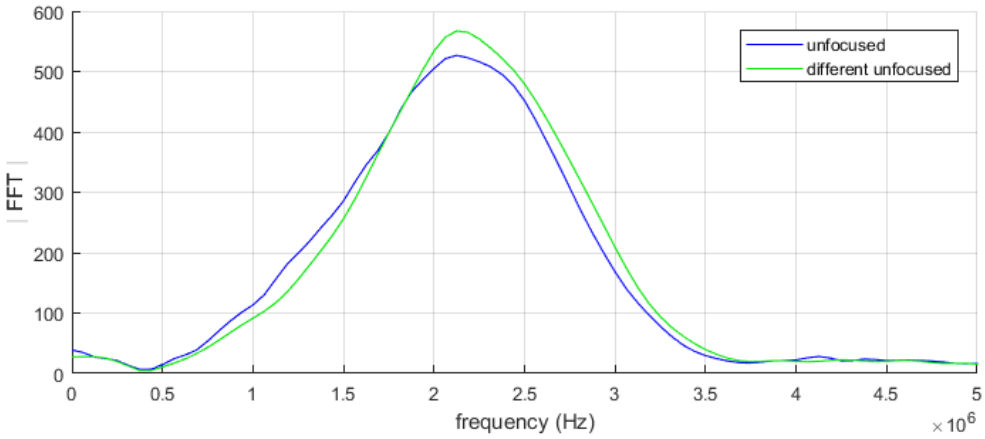

Figure 4.7: Spectra of the transmission measurement frequency spectra for identical transmitting but different receiving probes, all of unfocused 2.25 MHz frequency range.

The figure shows the frequency spectrum of the measured transmitted pulse for identical scenarios except that the receiving probe was replaced by another. All the probes used are of the unfocused, 2.25 MHz-centred type. The probes are available in focused and unfocused varieties, at different frequency ranges. However, these measurement results mean that two probes of the same type still have different frequency spectra i.e. P_1 as defined in Figure 4.3 is significantly different from P_2. This means that dividing the spectrum of a measured reflected pulse by a reference transmission pulse can induce significant error in the reflection coefficient spectrum due to the difference in probe spectra.

Figure 4.8 shows an example of transmission coefficient calculations for VeroWhite. In Figure 4.8a, the blue line represents the frequency spectrum of the reference pulse measured without a sample, while the red line represents the spectrum of the pulse transmitted through the 10 mm sample, measured with the same probes as the reference measurement. The spectrum of the sample transmission signal divided by the reference spectrum results in the transmission coefficient, which is plotted in Figure 4.8b.

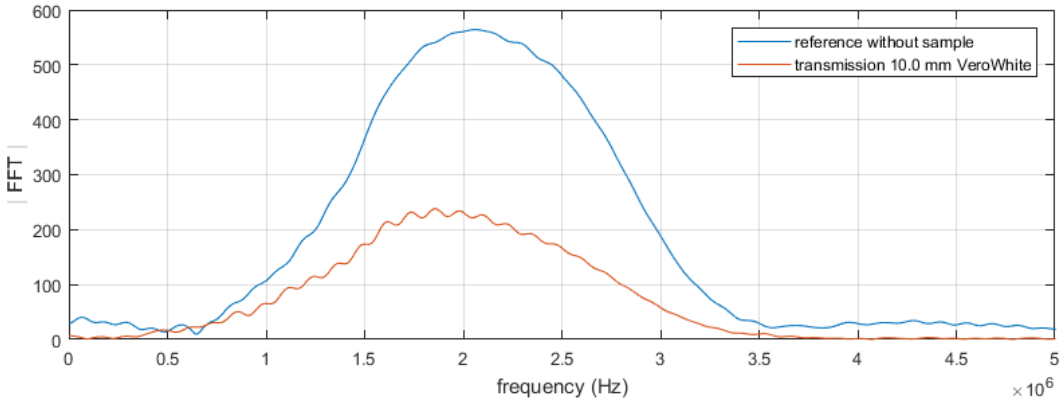

(a) Frequency spectra of the reference transmission pulse, and that of transmission with a 10 mm VeroWhite sample placed between the transducers.

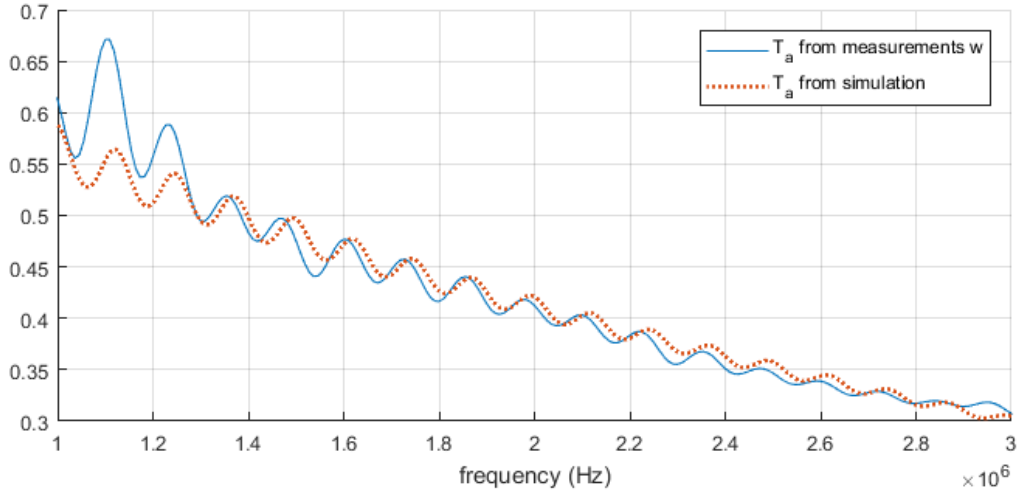

(b) Transmission coefficient for VeroWhite calculated from the spectra in (a), along with simulation results for comparison.

Figure 4.8: Transmission coefficient for 10 mm VeroWhite from measurement, along with simulation for comparison, and the spectra that the coefficient is calculated from.

Figure 4.8b shows the solid line of the absolute value of the amplitude transmission coefficient spectrum calculated from measurement. In the same plot is the predicted transmission coefficient for a simulation with parameters for VeroWhite. The thickness was set to 10.05 mm to better align the peaks in the plot, but this effect is minimal. The impedance and speed values used for VeroWhite in the simulation are those in Table 4.3. Finally, the attenuation coefficient was manually adjusted to a value of $\alpha = 15 + 31 \times 10^{-6} f$. Using these simulation parameters, the results are quite close to the coefficient calculated from measurements. The match is closer for frequencies that are more strongly present in the original signal, i.e. the simulation and measurement transmission coefficient match most closely around 2 MHz, which is the peak of the reference spectrum, and the match is poorer outside the 1.3-3.0 MHz range, because the signal is weaker outside this range.

Reflection and transmission coefficients were also calculated for two-layer sample measurements, to compare them to the model. Figure 4.9 shows the reflection coefficient calculated

from pulse-echo measurements of a two-layered sample of VeroWhite and Agilus Black of 3.0 mm each. Again, the best measurement range is from about 1.4-3.0 MHz because that is the strongest frequency range of the probe signal. R_a w and R_a b represent the VeroWhite and Agilus Black side, respectively, being closer to the transmitting probe. It can be seen that the reflection coefficients are significantly different depending on the orientation. The transmission coefficient is independent of orientation as predicted by the simulation, and a graph of this can be found in Appendix F.3.

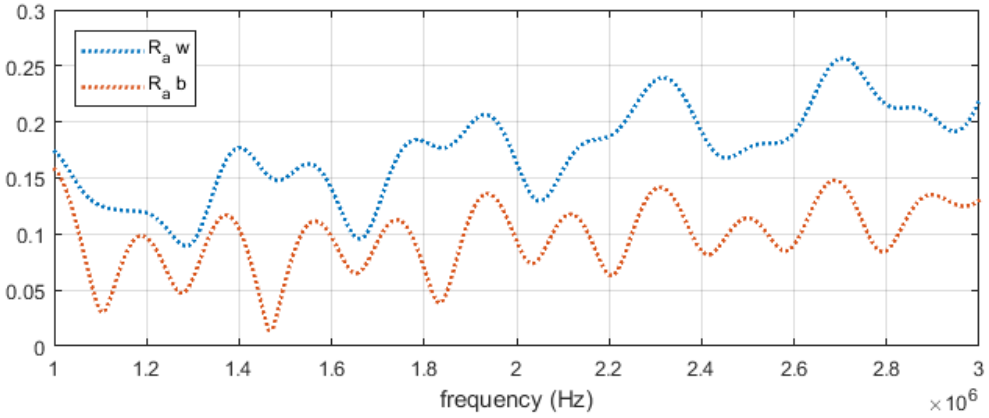

Figure 4.9: Reflection coefficient from measurement for two-layer sample of Agilus Black and VeroWhite, with reversal of side facing the transmitting transducer.

4.4 Measurements discussion

The characterisation results show that the available 3D print materials are in the wrong impedance range to be able to use in a coupling structure between, for example, PZT and water (which for a single layer would need an impedance of 6.66 MRayl, and both higher and lower values for more layers). Additionally, the individual values of the material impedances are still not close to the values required for the discretised exponential transition between VeroWhite and Agilus Black, especially because there are so few impedances midway between the two extreme impedances (see Figure 4.5b). Therefore, it was also not possible to make a layered structure with an optimal impedance transition from Agilus Black to VeroWhite.

If the possibility of printing customised proportions of two materials becomes possible, then this would improve the applicability of 3D printing for impedance matching lenses. In that case, care must be taken that the two materials are evenly distributed three-dimensionally, so that the resulting material may still be considered homogeneous. If not homogeneous, the model would need to be modified to describe inhomogeneous materials.

One limitation is that for each material, only the real speed of sound is determined, and it is taken to be independent of frequency within the relevant range. This neglects any dispersive effects, and also any imaginary component in sound speed. There was an attempt to calculate phase velocity for the materials based on the Fourier transform phases from measurements, but this resulted in unrealistic (wrong order of magnitude) numbers and was not looked into further due to time constraints.

The biggest challenge in the measurement processing was to extract attenuation coefficient values to characterise the materials and use in simulation. The Lommel diffraction integral made only small differences at some frequencies, of up to 10% of the α value, but this still did not help obtain a reliable approximation of the attenuation from measurements. The exact composition of the 3D print materials is unknown, but they are some type of viscoelastic, photo polymeric solid. One possibility is that the attenuation coefficient is a more complicated, multi-term higher-order function of frequency, and that this makes it more difficult to determine and approximate with a linear function.

Given the lack of relevant material properties published by Stratasys, a lot of time was spent characterising the materials, which may have otherwise been spent expanding the model. Nevertheless, the materials were characterised, and measurements were taken to compare with simulation results.

In all of the results from measurements, the values best agree with those from simulation at the frequencies at which the signal is strongest, i.e. around 2.25 MHz. There are probes available at higher frequencies, such as centred at 5 MHz. However, at these higher frequencies, the signal-to-noise ratio is much lower due to higher attenuation, and in some cases essential measurements like the back reflections were not discernible from noise, so these higher frequency measurements were not used.

Another remark is that the model describes reflections from the various interfaces at the sample, but it does not include any signals reflected off the walls of the water tanks. In the reflection measurements, smaller oscillations occur at twice the time of the first set of oscillations, due to portions of the first reflections reflecting off the glass walls of the water tank. These subsequent reflections are neglected in any measurement processing because they are not relevant to the model. Additionally, the effect of water absorption is considered negligible. This assumption was verified by comparing measurements immediately after submersion to those for a sample underwater for 30 minutes. Selected samples were also weighed before and after, and no significant change was found.

The calculation of the transmission coefficient seemed effective, based on comparison of measured results to simulated results. However, as indicated in Figure 4.7, the individual probes have significantly different frequency characteristics, despite being of the same probe type. This means that a reflection measurement involving twice the same probe P_1 is divided by a reference through-transmission measurement using two probes, P_1 and P_2. This does not change the behaviour of the reflection coefficient oscillations and the locations of peaks and troughs, but it does affect the magnitude and overall trend of the reflection coefficient. For instance, in Figure 4.9, the reflection coefficients slope upward with increase in frequency, while the model for a comparable setup predicts that there is no such increase (in Figure 3.3).

It is possible to obtain a reference reflection measurement with twice the same probe in a different setup, using a divided tank in which the second half may contain air or water. When containing air, this would create a full reflection for reference. The sample can be placed in the division, and when the other half is filled with water, this can be used for a reflection measurement. [60, p. 50] However, this setup was not available in this particular work.

4.5 Conclusions

We have developed a measurement method and data processing scheme that allows us to determine the acoustic impedance and speed of sound in the various materials that can be printed by the Eden 260 3D printer. Our results show that the range of impedances is 2.30 to 2.99 MRayl. This range is too small and too low to fabricate impedance matching structures between the ultrasound probe and water or tissue.

Chapter 5

Overall discussion and conclusion

Using the transfer matrix method, a model has been developed that can be used to predict the reflection and transmission of a wave, for an object consisting of n number of plates, all with a specific speed of sound and frequency-dependent damping. The model is able to capture the behaviour of a single layer reasonably well, as shown by comparing measured and simulated transmission coefficient results in Figure 4.8b. The model is validated in the 1.4-3.0 MHz range, because the 2.25 MHz-centred probes used, have the strongest signal for these frequencies.

For multiple layers, the model fits two important additional aspects: the transmission coefficient can be considered independent of the orientation (i.e. which side is closest to the transmitting transducer), and the reflection coefficient does depend on this orientation. This can be seen by comparing Figures 4.9 and F.4 from measurements to the predictions for the equivalent setup from simulations in Figure 3.3. In the transmission coefficient, there are few discernible features, but nevertheless there are similarities.

The changes with frequency are much better discernible in the reflection coefficients than the transmission coefficients for the frequencies and materials used. Again, the simulation and the values calculated from measurements show good correspondence in the shapes and locations of the oscillation peaks and troughs. However, the actual values and the general trend are off. As mentioned, this is expected to be caused by two factors: the mismatch in probes in reflection measurements to the reference, and the difficulty in fitting the model to the measured data for attenuation coefficient.

The α values calculated from measurement result in error ranges in the order of $10\,\mathrm{m}^{-1}$, but the model is sensitive in the order of $10\,\mathrm{m}^{-1}$ in both slope and intercept. In other words, while the measured values have a standard deviation in the order of 10%, the simulation requires an accuracy in the order of 1%. Additionally, the linear model may be too simple. For example, frequency terms of higher orders may occur, referring to equation 2.7, and the trend in Figure 4.6 is not necessarily a straight line, considering the error margins.

Having reasoned through differences in the general trend and the exact values of the transmission and reflection coefficients between simulation and measurement, the model has been shown to be effective in the cases examined: relatively simple structures with few layers, and with acoustic impedance relatively close to water.

Scattering is one phenomenon not taken into account in the simulation, and this may contribute to mismatch between simulated and measured values. The materials may have

been dispersive, but this was modelled as having a single phase velocity equal to the group velocity. However, it is likely that the phase velocity varies with frequency to some extent.

Another point that can use more consideration is the effect of complex impedances and sound speeds. This is because complex propagation constants were used to model attenuating materials, but only real densities and speeds were measured, resulting in real impedance values.

The model showed that an optimal transmission at a relatively wide range of frequencies could be achieved by using layers with an exponential impedance profile to match impedances between to materials. The model also showed that small percentages of deviation from the optimal impedances can still cause significant reduction in the antireflection effect, so it is important to find the right materials and production method to apply these concepts. With the 3D printer used in this work, it is not yet feasible to print an antireflection lens for interfaces like PZT-water, because of limitations in print materials and mix proportion flexibility. However, the exponential impedance profile combined with speed-dependent thickness is worth investigating further, including with developments in materials and other manufacture methods. This can eventually lead to improved efficiency and effectiveness of practical ultrasound applications.

5.1 Recommendations

Based on this work, a number of improvements and further investigations can be made.

Firstly, the model could be validated more extensively. Characterisation measurements can be repeated more times to perform better error analysis. The experiments can also be done for materials with acoustic impedance much higher than that of water, because the range of impedances for which the model is validated is relatively small, especially considering piezoelectric material impedances. Additionally, the model has also not been validated for optimal impedances, so given the right materials, this can be done to examine this aspect of the simulations. Other methods of determining attenuation and dispersion from measurements can also be looked into. Another aspect to look into for measurements is to find methods of determining complex speeds of sound and/or density.

The model itself can also be expanded to describe oblique incidence, multiple modes, and finite structures which are relevant at lower frequencies. The effect of complex impedance and of dispersion may be useful to explore, as well as non-planar waves and beam-shaping. This can allow the results to be used in more varied applications, where reduced reflections can improve performance.

Appendix A

Trigonometric functions and complex exponentials

The relations between circular and hyperbolic trigonometric functions and their exponential forms are used to relate transfer matrices of lossless and lossy media. These relations are shown in equation A.1.

$$\sin\theta = \frac{1}{2j}(e^{j\theta} - e^{-j\theta}) \tag{A.1a}$$

$$\cos\theta = \frac{1}{2}(e^{j\theta} + e^{-j\theta}) \tag{A.1b}$$

$$\sinh\theta = \frac{1}{2}(e^{\theta} - e^{-\theta}) \tag{A.1c}$$

$$\cosh\theta = \frac{1}{2}(e^{\theta} + e^{-\theta}) \tag{A.1d}$$

Appendix B

Acoustically relevant properties of selected materials

Table B.1 shows the longitudinal speed of sound and the specific acoustic impedance for several materials to provide context better context to this work. The materials are taken to be at 20°C. It can be seen that the impedance of air is several degrees of magnitude lower than that of all the other materials listed, which shows why, for example, air needs to be eliminated from a transducer-tissue coupling. Soft tissue has an impedance range close to that of water, while hard solids like PZT and steel have relatively high impedances.

Table B.1: Speed of sound and specific acoustic impedance for selected materials [61, p. 270] [62, p. 678].

Material	Speed ($\mathrm{m\,s^{-2}}$)	Impedance (MRayl)
water	1480	1.48
air	330	0.0004
PZT	3800	30.0
stainless steel	3300	47.0
soft tissue	1440-1640	1.3-1.7
bone	4080	6.0

Appendix C

Derivations

C.1 Derivation of TMM

In this part, it is shown how the transfer matrix relates the state variables at two points in space. Within a single material with propagation constant γ and (complex) characteristic impedance z_l, the sound pressure and particle velocity, which are the state variables, are expressed at two different x coordinates as shown in the table below.

	$x = x_1$	$x = x_2$
p	$(Ae^{-\gamma x_1} + Be^{\gamma x_1})e^{j\omega t}$	$(Ae^{-\gamma x_2} + Be^{\gamma x_2})e^{j\omega t}$
v	$\frac{1}{z_l}(Ae^{-\gamma x_1} - Be^{\gamma x_1})e^{j\omega t}$	$\frac{1}{z_l}(Ae^{-\gamma x_2} - Be^{\gamma x_2})e^{j\omega t}$

Let $x_2 = x_1 + d$. Then, it can be shown that p_1 is a linear combination of p_2 and v_2.

$$\cosh(\gamma d) \cdot p_2 + z_l \sinh(\gamma d) \cdot v_2 \tag{C.1}$$

Rewriting the hyperbolic functions to their exponential forms:

$$= \frac{1}{2}\left(e^{\gamma d} + e^{-\gamma d}\right) p_2 + \frac{z_l}{2}\left(e^{\gamma d} - e^{-\gamma d}\right) v_2 \tag{C.2}$$

Multiplying out:

$$= \frac{1}{2}\left[Ae^{-\gamma x_1 + j\omega t} + Be^{\gamma(x_1+2d)+j\omega t} + Ae^{-\gamma(x_1+2d)+j\omega t} + Be^{\gamma x_1 + j\omega t}\right] \tag{C.3}$$
$$+\frac{z_l}{2}\frac{1}{z_l}\left[Ae^{-\gamma x_1 + j\omega t} - Be^{\gamma(x_1+2d)+j\omega t} - Ae^{-\gamma(x_1+2d)+j\omega t} + Be^{\gamma x_1 + j\omega t}\right]$$

The $2d$ terms cancel out by subtraction, leaving the following:

$$= \frac{1}{2}\left[2Ae^{-\gamma x_1 + j\omega t} + 2Be^{\gamma x_1 + j\omega t}\right] \tag{C.4}$$

$$= p_1$$

This shows that the first line of the transfer matrix in equation 2.31 is correct. The second line can be verified in a similar manner, so this will not be written out here.

C.2 Geometric mean impedance matching

In this section, the layer impedance value resulting in maximum or minimum reflection at a quarter layer thickness is derived. Here, z_c represents the layer impedance.

First, the reflection coefficient is expressed in terms of the lossless transfer matrix elements, using equations 2.34 and 2.32. When the trigonometric functions are expressed in their exponential form and like terms are gathered, it results in the following:

$$R_a = \frac{\left(z_R - z_L + z_c - \frac{z_L z_R}{z_c}\right) e^{jkd} + \left(z_R - z_L - z_c + \frac{z_L z_R}{z_c}\right) e^{jkd}}{\left(z_R + z_L + z_c + \frac{z_L z_R}{z_c}\right) e^{jkd} + \left(z_R + z_L - z_c - \frac{z_L z_R}{z_c}\right) e^{jkd}} \tag{C.5}$$

When $d = \frac{\lambda}{4}$, kd becomes $\frac{\pi}{2}$. Filling this into the exponential terms:

$$R_a = \frac{\left(z_R - z_L + z_c - \frac{z_L z_R}{z_c}\right) j - \left(z_R - z_L - z_c + \frac{z_L z_R}{z_c}\right) j}{\left(z_R + z_L + z_c + \frac{z_L z_R}{z_c}\right) j - \left(z_R + z_L - z_c - \frac{z_L z_R}{z_c}\right) j} \tag{C.6}$$

By removing terms which are eliminated by subtraction, and simplifying:

$$R_a = \frac{z_c^2 - z_L z_R}{z_c^2 + z_L z_R} \tag{C.7}$$

By setting the numerator of equation C.7 to zero, it can be seen that the reflection equals zero when $z_c^2 = z_L z_R$, and assuming positive impedances, $z_c = (z_L z_R)^{\frac{1}{2}}$. Figure C.1 shows both these optimisation results for the single layer: for the different thicknesses, transmission is maximum at (odd multiples of) quarter wavelength thickness, and among the various impedances, transmission is maximised (and reflection minimised) for the geometric mean $z_c = (z_L z_R)^{\frac{1}{2}}$.

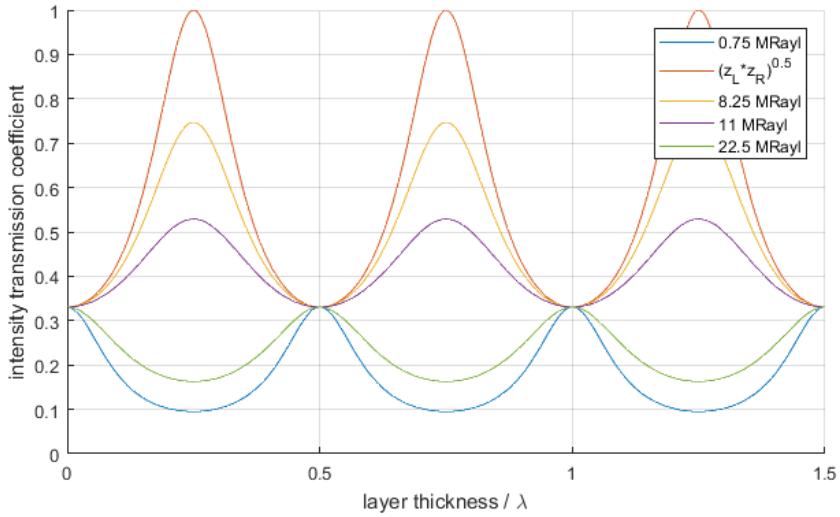

Figure C.1: Simulation of varying the single layer impedance for different layer thicknesses, with $z_L = 1.5$ MRayl and $z_R = 15$ MRayl. The legend shows layer impedance.

Appendix D

Additional figures from simulation

In this Appendix, some figures and discussions of simulation results are presented which are not crucial to the main work, but provide supporting information and context.

D.1 Single lossless layer between two identical media

When the left and right medium impedances, z_L and z_R are the same, a layer placed between them can only decrease transmission, or leave it unchanged, depending on the layer thickness. In this case, at thickness of $d = \frac{\lambda}{4}$, transmission is at a minimum, as seen in Figure D.1. Transmission is lower for layer impedances further from the boundary impedances, and this is similar to the result of when layer impedance lies outside the range of two unequal left and right impedances, plotted in Figure C.1.

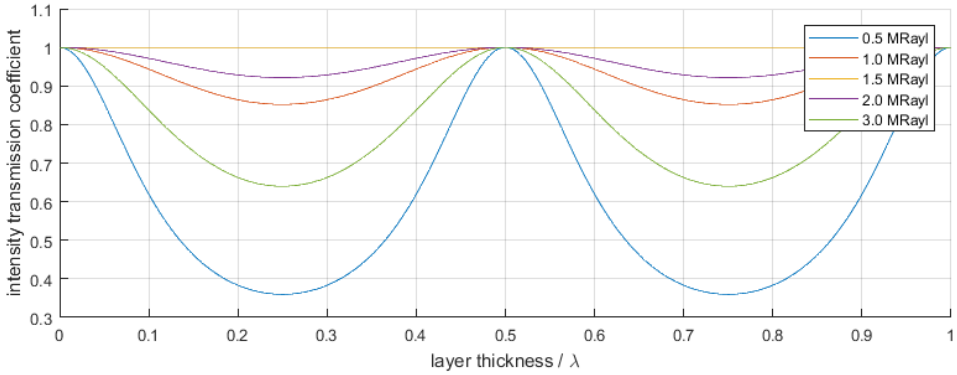

Figure D.1: Effect of varying the single layer impedance for different layer thicknesses, between two identical media $z_L = z_R = 1.5$ MRayl.

D.2 Amplitude reflection and transmission coefficients for single lossless layer

The amplitude reflection and transmission coefficients are complex numbers, of which the real part describes the magnitude of the oscillations, while the imaginary part describes the

phase. However, a negative real part also indicates that the wave is out of phase with the incident wave. Another consideration is that by the conservation of energy, the amplitude reflection coefficient cannot be greater than unity (positive or negative), because that would mean the reflected wave carries more energy than the incident wave. On the contrary, the amplitude transmission coefficient may be greater than one, because intensity also scales with impedance of the medium (equation 2.25).

An example of the intensity T and R values, along with the real and imaginary parts of the amplitudes coefficients, is plotted in Figure D.2. A number of variables can be changed to affect the plot. Changing the wavenumber k of the rightmost medium has no effect on the intensity coefficients, but it affects the periodicity of the amplitude transmission coefficients. Specifically, it is the ratio of right-medium wavenumber to layer-wavenumber which matters, and was chosen as 1.5 in the plot.

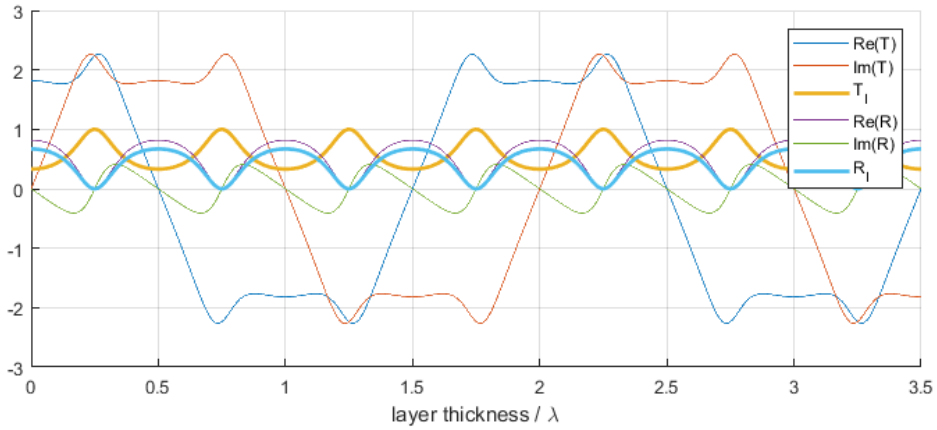

Figure D.2: Amplitude and intensity transmission and reflection coefficient values, for different thicknesses of a single lossless layer with optimal impedance; $z_L = 1.5$ MRayl and $z_R = 15$ MRayl.

As the focus is on optimising the energy transmission from one medium to another, the remaining simulations will concern the intensity transmission coefficient rather than the amplitude.

D.3 Two-layered attenuating sample

Figure D.3 shows the simulated values of reflection coefficient for a two-layered absorptive sample surrounded by water, with the same parameters and notation as used in Figure 3.3. It shoes that the reflection coefficient approaches a particular value at high frequencies, and that this value depends on the orientation of the sample. When, for example, the VeroWhite layer is closer to the transmission probe, the reflection coefficient approaches that of a single water-VeroWhite interface as calculated from the impedance values, using equation 2.27 (for normal incidence).

When there is no attenuation, there are two differences: the orientation no longer has effect, and the reflection coefficient does not approach any particular value at high frequencies.

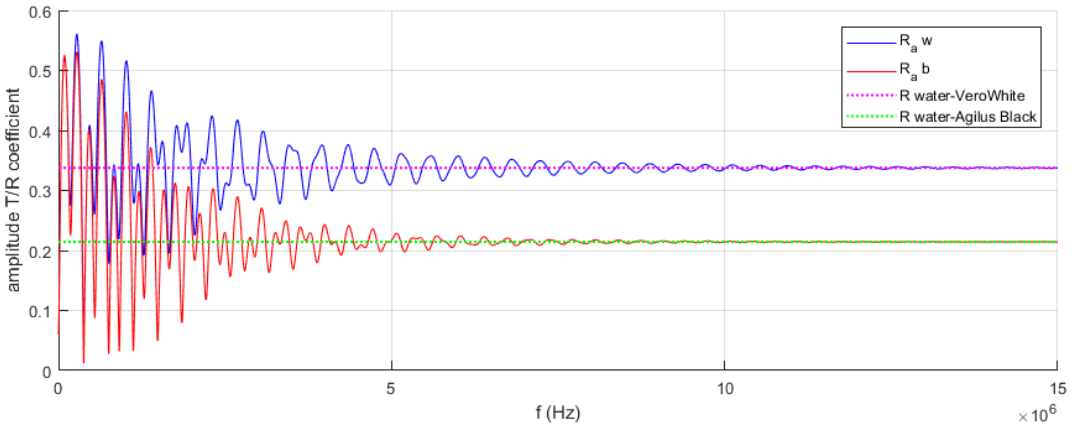

Figure D.3: Simulated transmission and reflection coefficients for a two-layered sample in water, in forward and reverse orientation, showing limiting behaviour at high frequencies.

Appendix E

Additional measurement data

Table E.1 shows the thicknesses in mm of the various single-material samples printed. All the samples have 5.0×5.0 mm^2 cross-sections. When two thicknesses are listed, this indicates two separate samples with different thicknesses of the same material. The more flexible materials are generally printed thinner than the rigid materials because they have higher attenuation, which sometimes makes measurements invalid if for example, the back reflection is no longer measurable because it is damped out. For multi layered samples, the main one used is a two-layered sample of pure VeroWhite and Agilus Black of 3.0 mm each. Other samples with more layers were printed, but results from these particular measurements are not insightful into the model because of heavy damping and mismatched kd, which for example leaves almost no oscillation or discernible features in reflection and transmission coefficients.

Table E.1: Table listing the various single-layer samples that were used.

Material	Thickness (mm)	Material	Thickness (mm)
Agilus Black	4.0, 10.0	RGD8530-DM	4.0, 10.0
FLX9840-DM	4.0	RGD8525-DM	6.0
FLX9850-DM	4.0, 6.0	RGD8520-DM	6.0, 10.0
FLX9860-DM	4.0	RGD8515-DM	6.0
FLX9870-DM	4.0	RGD8510-DM	6.0, 10.0
FLX9885-DM	4.0, 10.0	RGD8505-DM	6.0
FLX9895-DM	4.0	VeroWhite	6.0, 10.0

In table E.2, the results of time difference between front and back reflections are shown. These are calculated from the autocorrelation of the analytic signal, as described in section 4.2. Some comments are pertinent to these results.

Firstly, for several measurements at the higher frequency, the back surface reflection is indistinguishable from the noise, leading to fewer data points. Most notably this is with sound passing through Agilus Black along the x/y-axis, for which none of the measurements was valid at the higher frequency. Additionally, for this sample, the standard deviation is about an order of magnitude greater than for the other samples, which contributes to this print orientation being discarded for further investigation. Finally, the time differences are very similar, taking into account the standard deviation values, for the first two materials

in the table at the frequencies measured. Subsequently, the speed of sound is considered to be independent of frequency at the ranges relevant to this work.

Table E.2: Overview of selected measurement results for time difference between front and back reflection, thickness 10 mm.

material	frequency (MHz)	number of points	mean time difference (10^{-6} s)	standard deviation time diff. (10^{-6} s)
VeroWhite	2.5	8	7.98	0.041
	5	6	7.97	0.018
Agilus Black through z-axis	2.5	8	9.73	0.034
	5	3	9.75	0.071
Agilus Black through x/y-axis	2.5	8	9.69	0.302
	5	-	-	-

Appendix F

Additional figures from measurements

In this Appendix, some figures and discussions of measurement setup and results are presented which are not crucial to the main work, but provide supporting information and context.

F.1 Photographs of underwater ultrasound equipment

Figure F.1 is a photograph of the measurement setup illustrated schematically in Figure 4.1. It shows the wave pulser on the left, the water tank in the middle and the laptop on the right. The oscilloscope is partially obscured, behind the water tank. Also visible in this image are the rails on which distances are marked for suspending the clamp, and the slot in which an ultrasound probe is inserted on the visible face of the tank. The laptop is opened to the oscilloscope software.

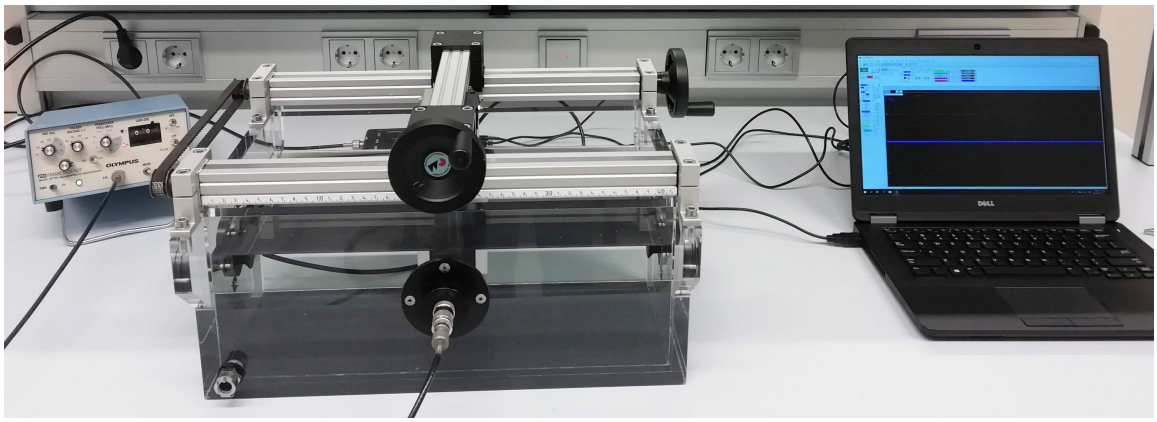

Figure F.1: Photograph of the water tank setup for ultrasound measurements.

Figure F.2 is a photograph of the ultrasound probes on the left, and of clamps holding four samples at the bottom. The ultrasound probes have BNC connectors on one end, and removable red protective caps at the other. The clamps can be opened to change the sample

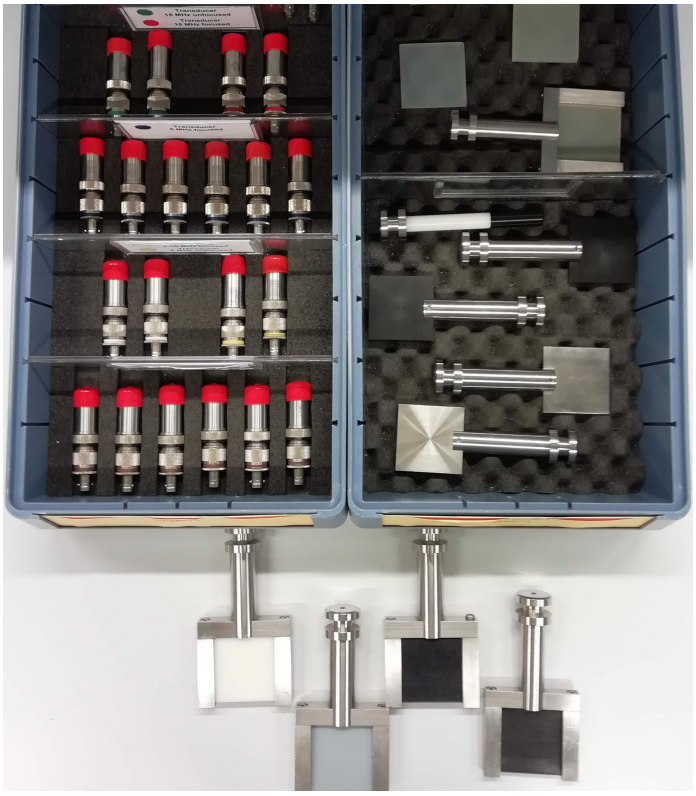

Figure F.2: Photograph of ultrasound probes and clamps with samples.

by removing two screws.

F.2 Varying the sample-transducer distance

Figure F.3 shows the effect of moving a block further from the ultrasound transducer. Four sets of measurements are plotted in total: the front and reverse orientation of the block at each of two distances. A slight time-difference at each front-reverse set would be because the probe-to-block distance differed by a fraction of a millimetre. A number of other observations can be made from this figure.

The reflections occur in pairs as front-face reflection and then back-face reflection. An increase in distance consistently increases the time for each of these reflections. Additionally, there are also recurring reflections between the probe and the block, which show as later oscillations (the first set occurred before 2×10^{-4} s and the second set after this time). These amplitudes from any given measurement get progressively smaller with time because of attenuation. Furthermore, the amplitude of reflections from the reverse face are slightly smaller than from the front face, which is more visible in the later reflections. The front face was visibly shinier than the reverse face, which means the reflections were probably more specular than the reverse face. With the reverse face towards the transducer, the sound must have gotten more scattered. However, the effect was minimal. Scattering from the surface was considered negligible, and not taken into account in the model.

Finally, no consistent differences, for example arising from beam shape, were found in

results (such as sound speed) computed from measurements at different distances.

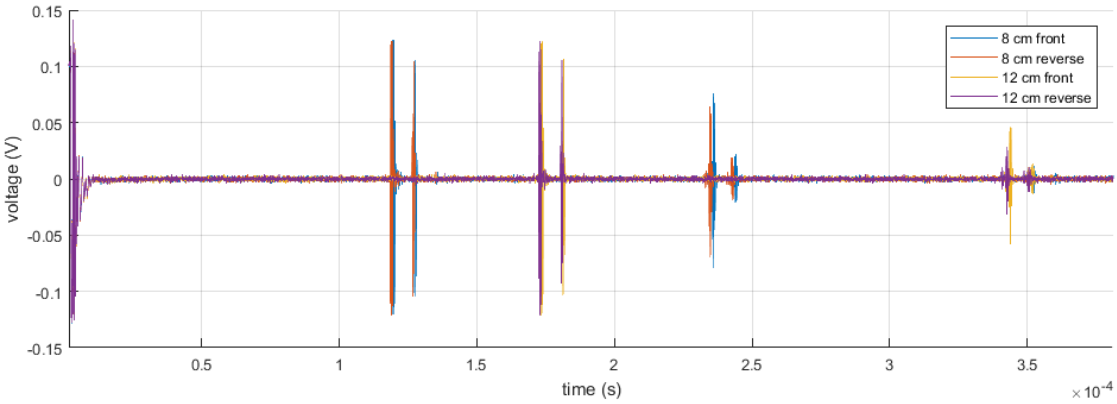

Figure F.3: Echos measured off block of VeroWhite placed 8 cm and 12 cm from the transducer, showing time-shift effect.

F.3 Transmission coefficient from measurement for two-layer sample

Figure F.4 shows a plot of the transmission coefficient calculated from through measurement with the two-layered VeroWhite, Agilus Black sample for reversal of the material closest to the transmitting probe. Accounting for noise, these two plots can be considered in the frequency range of the probes, which is about 1.4-3.0 MHz. Comparing to the simulation results in Figure 3.3, there are corresponding peaks and troughs, such as the minima at 1.4 MHz and around 2.3 MHz.

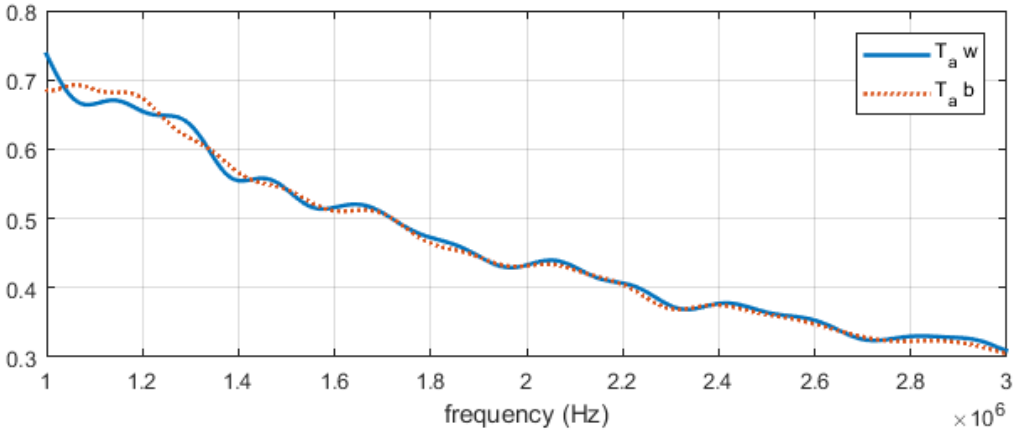

Figure F.4: Transmission coefficient from measurement for two-layer sample of Agilus Black and VeroWhite, with reversal of side facing the transmitting transducer.

Bibliography

[1] T. A. Whittingham, "Broadband transducers," *European radiology*, vol. 9, pp. 298–303, 1999.

[2] J. E. Aldrich, "Basic physics of ultrasound imaging," *Critical care medicine*, vol. 35, no. 5, pp. S131–S137, 2007.

[3] C. Fei, J. Ma, C. T. Chiu, J. A. Williams, W. Fong, Z. Chen, B. Zhu, R. Xiong, J. Shi, T. K. Hsiai, K. K. Shung, and Q. Zhou, "Design of matching layers for high-frequency ultrasonic transducers," *Applied physics letters*, vol. 107, p. 123505, 9 2015.

[4] Q. Zhou, K. H. Lam, H. Zheng, W. Qiu, and K. K. Shung, "Piezoelectric single crystal ultrasonic transducers for biomedical applications," *Progress in materials science*, vol. 66, pp. 87–111, 2014.

[5] C. S. DeSilets, J. D. Fraser, and G. S. Kino, "The design of efficient broad-band piezoelectric transducers," *IEEE Transactions on Sonics and Ultrasonics*, vol. 25, no. 3, pp. 115–125, 1978.

[6] J. Souquet, P. Defranould, and J. Desbois, "Design of low-loss wide-band ultrasonic transducers for noninvasive medical application," *IEEE transactions on sonics and ultrasonics*, vol. 26, no. 2, pp. 75–80, 1979.

[7] H. J. Fang, Y. Chen, C. M. Wong, W. B. Qiu, H. L. W. Chan, J. Y. Dai, Q. Li, and Q. F. Yan, "Anodic aluminum oxide–epoxy composite acoustic matching layers for ultrasonic transducer application," *Ultrasonics*, vol. 70, pp. 29–33, 2016.

[8] T. Manh, A.-T. T. Nguyen, T. F. Johansen, and L. Hoff, "Microfabrication of stacks of acoustic matching layers for 15 MHz ultrasonic transducers," *Ultrasonics*, vol. 54, no. 2, pp. 614–620, 2014.

[9] S. Saffar and A. Abdullah, "Determination of acoustic impedances of multi matching layers for narrowband ultrasonic airborne transducers at frequencies below 2.5MHz – Application of a genetic algorithm," *Ultrasonics*, vol. 52, no. 1, pp. 169–185, 2012.

[10] L. Bai, H. Y. Dong, G. Y. Song, Q. Cheng, B. Huang, W. X. Jiang, and T. J. Cui, "Impedance-Matching Wavefront-Transformation Lens Based on Acoustic Metamaterials," *Advanced Materials Technologies*, vol. 0, p. 1800064, 7 2018.

[11] Z. Li, D.-Q. Yang, S.-L. Liu, S.-Y. Yu, M.-H. Lu, J. Zhu, S.-T. Zhang, M.-W. Zhu, X.-S. Guo, H.-D. Wu, X.-L. Wang, and Y.-F. Chen, "Broadband gradient impedance matching using an acoustic metamaterial for ultrasonic transducers," *Scientific Reports*, vol. 7, p. 42863, 2 2017.

[12] W. H. Southwell, "Gradient-index antireflection coatings," *Optics Letters*, vol. 8, no. 11, pp. 584–586, 1983.

[13] Y. Matsuoka, S. Mathonnèire, S. Peters, and W. T. Masselink, "Broadband multilayer anti-reflection coating for mid-infrared range from 7 μm to 12 μm," *Applied optics*, vol. 57, no. 7, pp. 1645–1649, 2018.

[14] M. C. Ziskin, "Fundamental physics of ultrasound and its propagation in tissue.," *Radiographics*, vol. 13, no. 3, pp. 705–709, 1993.

[15] S. E. Kentish, "Engineering Principles of Ultrasound Technology," *Ultrasound: Advances for Food Processing and Preservation*, pp. 1–13, 1 2017.

[16] D. Ensminger and L. J. Bond, *Ultrasonics: Fundamentals, Technologies, and Applications, Third Edition*. Mechanical Engineering, CRC Press, 2011.

[17] J. A. Gallego-Juárez and K. F. Graff, "1 - Introduction to power ultrasonics," in *Applications of High-Intensity Ultrasound*, pp. 1–6, Oxford: Woodhead Publishing, 2015.

[18] G. ter Haar and C. Coussios, "High intensity focused ultrasound: physical principles and devices," *International Journal of Hyperthermia*, vol. 23, no. 2, pp. 89–104, 2007.

[19] L. Svilainis and G. Motiejūnas, "Power amplifier for ultrasonic transducer excitation," *Ultragarsas Ultrasound*, vol. 58, no. 1, pp. 30–36, 2006.

[20] N. Ghasemi, N. Abedi, and G. Mokhtari, "Real-time method for resonant frequency detection and excitation frequency tuning for piezoelectric ultrasonic transducers," in *Power Engineering Conference (AUPEC), 2016 Australasian Universities*, pp. 1–5, IEEE, 2016.

[21] J. Krautkrämer and H. Krautkrämer, *Ultrasonic Testing of Materials*. Allan and Unwin, 1969.

[22] H. Kuttruff, *Ultrasonics: Fundamentals and Applications*. Springer Netherlands, 2012.

[23] D. Dowsett, P. A. Kenny, and R. E. Johnston, *The Physics of Diagnostic Imaging Second Edition*. A Hodder Arnold Publication, Taylor & Francis, 2006.

[24] M. A. Fink and J.-F. Cardoso, "Diffraction effects in pulse-echo measurement," *IEEE transactions on sonics and ultrasonics*, vol. 31, no. 4, pp. 313–329, 1984.

[25] P. H. Rogers and A. L. Van Buren, "An exact expression for the Lommel diffraction correction integral," *The Journal of the Acoustical Society of America*, vol. 55, pp. 724–728, 4 1974.

[26] M. K. Feldman, S. Katyal, and M. S. Blackwood, "Ultrasound Artifacts," *RadioGraphics*, vol. 29, pp. 1179–1189, 7 2009.

[27] R. Barr, Hindi, and Peterson, "Artifacts in diagnostic ultrasound," *Reports in Medical Imaging*, p. 29, 6 2013.

[28] C. Shera, J. Rosowski, K. Stevens, and L. Braida, "The Quantification of Sound and the Wave Equation," *6.551J Acoustics of Speech and Hearing*, 2004.

[29] R. K. Hobbie and B. J. Roth, *Intermediate Physics for Medicine and Biology*. Springer International Publishing, 2015.

[30] Z. Nazarchuk, V. Skalskyi, and O. Serhiyenko, "Propagation of Elastic Waves in Solids," in *Acoustic Emission: Methodology and Application*, Foundations of Engineering Mechanics, pp. 29–73, Springer International Publishing, 2017.

[31] R. L. Smith, "The effect of grain size distribution on the frequency dependence of the ultrasonic attenuation in polycrystalline materials," *Ultrasonics*, vol. 20, no. 5, pp. 211–214, 1982.

[32] C. Lane, *The development of a 2D ultrasonic array inspection for single crystal turbine blades*. Springer Science & Business Media, 2013.

[33] R. W. B. Stephens and A. E. Bate, *Acoustics and Vibrational Physics*. Edward Arnold, 1966.

[34] L. Brillouin, *Wave Propagation and Group Velocity*. Pure and applied physics, Academic Press, 1960.

[35] V. Gerasik and M. Stastna, "Complex group velocity and energy transport in absorbing media," *Physical Review E*, vol. 81, no. 5, p. 56602, 2010.

[36] L. Muschietti and C. T. Dum, "Real group velocity in a medium with dissipation," *Physics of Fluids B: Plasma Physics*, vol. 5, pp. 1383–1397, 5 1993.

[37] R. P. Feynman, R. B. Leighton, and M. Sands, *The Feynman Lectures on Physics, Vol. I: The New Millennium Edition: Mainly Mechanics, Radiation, and Heat*. Basic Books, 2015.

[38] G. B. Deane, "Internal friction and boundary conditions in lossy fluid seabeds," *Journal of the Acoustical Society of America*, vol. 101, pp. 233–240, 1 1997.

[39] F. Jacobsen and P. M. Juhl, *Fundamentals of General Linear Acoustics*. Wiley, 2013.

[40] F. Simonetti and P. Cawley, "Ultrasonic interferometry for the measurement of shear velocity and attenuation in viscoelastic solids," *The Journal of the Acoustical Society of America*, vol. 115, no. 1, pp. 157–164, 2004.

[41] R. N. Bracewell and R. N. Bracewell, *The Fourier transform and its applications*, vol. 31999. McGraw-Hill New York, 1986.

[42] P. L. D. Peres, I. S. Bonatti, and A. Lopes, "Transmission Line Modeling: A Circuit Theory Approach," *SIAM Review*, vol. 40, no. 2, pp. 347–352, 1998.

[43] T. L. Szabo, *Diagnostic Ultrasound Imaging: Inside Out*. Biomedical Engineering, Elsevier Science, 2004.

[44] B. H. Song and J. S. Bolton, "A transfer matrix approach for estimating the characteristic impedance and wave numbers of limp and rigid porous materials," *The Journal of the Acoustical Society of America*, vol. 107, no. 3, pp. 1131–1152, 2000.

[45] C. Gomez-Reino, J. Linares, and J. Sochacki, "Image and transform transmission through a GRIN rod with exponential variation of the equi-index surfaces," *Applied optics*, vol. 25, no. 7, pp. 1076–1078, 1986.

[46] J. W. Leem and J. S. Yu, "Multi-functional antireflective surface-relief structures based on nanoscale porous germanium with graded refractive index profiles," *Nanoscale*, vol. 5, no. 6, pp. 2520–2526, 2013.

[47] C. Zwikker, *Fysische materiaalkunde*. No. v. 1 in Fysische materiaalkunde, Wetenschappelijke Uitg. Mij., 1966.

[48] M. Nad, "Ultrasonic horn design for ultrasonic machining technologies," *Applied and Computational Mechanics*, vol. 4, pp. 79–88, 2010.

[49] M. G. L. Roes, J. L. Duarte, and M. A. M. Hendrix, "Design of stepped exponential horns for acoustic energy transfer systems," in *Ultrasonics Symposium (IUS), 2013 IEEE International*, pp. 306–309, IEEE, 2013.

[50] G. Kossoff, "The effects of backing and matching on the performance of piezoelectric ceramic transducers," *IEEE Transactions on sonics and ultrasonics*, vol. 13, no. 1, pp. 20–30, 1966.

[51] D. Rhazi and N. Atalla, "A simple method to account for size effects in the transfer matrix method," *The Journal of the Acoustical Society of America*, vol. 127, pp. EL30–EL36, 1 2010.

[52] W. T. Thomson, "Transmission of Elastic Waves through a Stratified Solid Medium," *Journal of Applied Physics*, vol. 21, pp. 89–93, 2 1950.

[53] O. Dazel, J.-P. Groby, B. Brouard, and C. Potel, "A stable method to model the acoustic response of multilayered structures," *Journal of Applied Physics*, vol. 113, no. 8, p. 83506, 2013.

[54] Stratasys Ltd., "Objet Eden260VS Datasheet," 2015.

[55] Olympus Corp., "Panametrics-NDT Ultrasonic Transducers Datasheet," 2016.

[56] T. Cutard, D. Fargeot, C. Gault, and M. Huger, "Time delay and phase shift measurements for ultrasonic pulses using autocorrelation methods," *Journal of Applied Physics*, vol. 75, pp. 1909–1913, 2 1994.

[57] M. Feldman, "Hilbert transform in vibration analysis," *Mechanical Systems and Signal Processing*, vol. 25, no. 3, pp. 735–802, 2011.

[58] P. He and J. Zheng, "Acoustic dispersion and attenuation measurement using both transmitted and reflected pulses," *Ultrasonics*, vol. 39, no. 1, pp. 27–32, 2001.

[59] T. Pialucha and P. Cawley, "An investigation of the accuracy of oblique incidence ultrasonic reflection coefficient measurements," *The Journal of the Acoustical Society of America*, vol. 96, no. 3, pp. 1651–1660, 1994.

[60] M. A. G. Rodrigo, *The ultrasonic pulse-echo immersion technique and attenuation coefficient of particulate composites*. University of Rhode Island, 2013.

[61] P. P. L. Regtien and E. Dertien, *Sensors for Mechatronics*. Elsevier Science, 2018.

[62] A. Y. K. Chan, *Biomedical Device Technology: Principles and Design*. Charles C. Thomas, publisher, Limited, 2016.

Acknowledgements

I would like to thank the members of the examination committee for all their guidance, feedback and help: Martijn Schouten, Gijs Krijnen, Kees Slump and Herbert Wormeester. Additionally, Sander Smits was accommodating and supportive in his operation of the 3D printer. Henk van Dijk was kind enough to set up and arrange for measurement sessions, and Jolanda Boelema-Kaufmann provided valuable help in many practicalities. Additionally, I am grateful to all the others who contributed to this work in many small but significant ways.